Mon. Not. R. Astron. Soc. **395,** 1749–1767 (2009) doi:10.1111/j.1365-2966.2009.14664.x

Orbitally modulated dust formation by the WC7+O5 colliding-wind binary WR 140

P. M. Williams,[1⋆] S. V. Marchenko,[2] A. P. Marston,[3,4] A. F. J. Moffat,[5] W. P. Varricatt,[6] S. M. Dougherty,[7] M. R. Kidger,[4,8] L. Morbidelli[9] and M. Tapia[10]

[1]*Institute for Astronomy, Scottish Universities Physics Alliance, University of Edinburgh, Royal Observatory, Edinburgh EH9 3HJ*
[2]*Department of Physics and Astronomy, Western Kentucky University, 1906 College Heights Blvd #11077, Bowling Green, KY 42101, USA*
[3]*SIRTF Science Center, IPAC, Caltech, Mail Stop 314-6, Pasadena, CA 91125, USA*
[4]*Herschel Science Centre, European Space Astronomy Centre, Villafranca del Castillo, PO Box - Apdo.50727, 28080 Madrid, Spain*
[5]*Département de physique, Université de Montréal, C.P. 6128, Succ. Centre-Ville, Montréal, QC, H3C 3J7, Canada*
[6]*Joint Astronomy Centre, 660 N. A'ohōkū Place, Hilo, HI 96720, USA*
[7]*National Research Council of Canada, Herzberg Institute for Astrophysics, Dominion Radio Astrophysical Observatory, PO Box 248, Penticton, B.C. V2A 6J9, Canada*
[8]*Ingenieria y Servicios Aeroespaciales SA, ESAC, Villafranca del Castillo, PO Box - Apdo.50727, 28080 Madrid, Spain*
[9]*INAF - Osservatorio Astrofisico di Arcetri, Largo E. Fermi 5, I-50125 Firenze, Italy*
[10]*Universidad Nacional Autónoma de México, Instituto de Astronomía, Apartado Postal 877, Ensenada B.C., Mexico*

Accepted 2009 February 19. Received 2009 February 16; in original form 2008 December 22

ABSTRACT

We present high-resolution infrared (2–18 μm) images of the archetypal periodic dust-making Wolf–Rayet binary system WR 140 (HD 193793) taken between 2001 and 2005, and multi-colour (J – [19.5]) photometry observed between 1989 and 2001. The images resolve the dust cloud formed by WR 140 in 2001, allowing us to track its expansion and cooling, while the photometry allows tracking the average temperature and total mass of the dust. The combination of the two data sets constrains the optical properties of the dust, and suggests that they differ from those of the dust made by the WC9 dust-makers, including the classical 'pinwheel', WR 104. The photometry of individual dust emission features shows them to be significantly redder in (nbL'–[3.99]), but bluer in ([7.9]–[12.5]), than the binary, as expected from the spectra of heated dust and the stellar wind of a Wolf–Rayet star. The most persistent dust features, two concentrations at the ends of a 'bar' of emission to the south of the star, were observed to move with constant proper motions of 324 ± 8 and 243 ± 7 mas yr^{-1}. Longer wavelength (4.68 and 12.5 μm) images show dust emission from the corresponding features from the previous (1993) periastron passage and dust formation episode, showing that the dust expanded freely in a low-density void for over a decade, with dust features repeating from one cycle to the next. A third persistent dust concentration to the east of the binary (the 'arm') was found to have a proper motion ∼320 mas yr^{-1}, and a dust mass about one-quarter that of the 'bar'. Extrapolation of the motions of the concentrations back to the binary suggests that the eastern 'arm' began expansion four to five months earlier than those in the southern 'bar', consistent with the projected rotation of the binary axis and wind-collision region (WCR) on the sky. A comparison of model dust images and the observations constrains the intervals when the WCR was producing sufficiently compressed wind for dust nucleation in the WCR, and suggests that the distribution of this material was not uniform about the axis of the WCR, but more abundant in the following edge in the orbital plane.

Key words: circumstellar matter – stars: individual: WR 140 – stars: Wolf-Rayet – infrared: stars.

1 INTRODUCTION

In 1977, the infrared (IR) flux from HD 193793 (WR 140) was observed to have risen by almost an order of magnitude

⋆E-mail: pmw@roe.ac.uk

© 2009 The Authors. Journal compilation © 2009 RAS

(e.g. $\Delta L' \simeq 2.4$) in less than a year and to have developed a spectral energy distribution (SED) indicating the formation of circumstellar dust (Williams et al. 1978; Hackwell, Gehrz & Grasdalen 1979). Although infrared SEDs characteristic of heated circumstellar dust had previously been observed from WC8–9 type Wolf–Rayet stars (Allen, Harvey & Swings 1972; Gehrz & Hackwell 1974), HD 193793 was the first WR star to show evidence for the formation of circumstellar dust on a short time-scale. Subsequent observations showed the emission to fade as the dust cooled and then, in 1985, to rise again in another dust formation episode (Williams et al. 1990, hereafter Paper I). From the IR light curves, a photometric period of 2900 ± 10 d was derived, leading to a solution of the radial velocities which showed WR 140 to be a high-eccentricity ($e = 0.84$) WC7+O5[1] spectroscopic binary. The episodes of dust formation appear to coincide with periastron passage (Paper I).

In the interim, rises in IR emission indicative of episodes of dust formation were observed from two other WR stars, WR 48a (WC8–9) in 1978–79 (Danks et al. 1983) and WR 137 (WC7+O) in 1983–84 (Williams et al. 1985), showing that WR 140 was not unique, but rather a prototype of a class of episodic dust-making WR stars, of which we now know seven (Williams 2002).

The particular interest and problem posed by the episodic dust-making WR stars is the great difficulty of making dust in their winds, as pointed out in the case of WR 140 by Hackwell et al. (1979): the stellar winds are not sufficiently dense to allow homonuclear grain growth. The same problem was discussed in respect of the 'classical' dust-makers amongst the WC8–9 stars (Williams, van der Hucht & Thé 1987). Zubko (1998) found that carbon grains having a drift velocity relative to the WC8–9 wind could grow via collision with carbon ions, but the question of grain nucleation remains open. A chemical kinetic study of the formation of molecular species and carbon grain precursors in WC9 winds by Cherchneff et al. (2000) found that only C_2 was formed in useful amounts, and even that required significantly (a factor of 10^3) higher densities than expected in the regions of isotropic, smooth WR winds where dust grains are observed. Evidently, the observation of dust formation by WR stars requires that their winds contain regions of significantly higher density than expected in an isotropic smooth wind.

Large-scale, high-density structures are provided by compression of stellar winds in strong shocks formed where the wind of a WR star collides with that of a sufficiently luminous companion in a binary system – a colliding-wind binary (CWB) – as occurs in WR 140. Usov (1991) suggested that very high compression factors (10^3–10^4) could be produced in WR 140 if the heated and compressed wind was able to cool efficiently. The link between the dust formation episodes and binary orbit is provided by periodic increases by a factor of ~ 40 of the *pre-shock* wind density at the wind-collision region (WCR) for a brief time around periastron passage (Williams 1999). Although hydrodynamical modelling by Stevens, Blondin & Pollock (1992) found the collision region in WR 140 to be adiabatic, which would give much less compression, this does not hold very close to periastron, when the compressed wind material is observed to cool through additional emission components on low-excitation C III and He I lines (Marchenko et al. 2003, hereafter MM03; Varricatt, Williams & Ashok 2004, hereafter VWA). The cooling in the emission sub-peak on the He I λ1.083 μm line exceeds that by the X-rays (VWA).

Other high-density structures which could aid dust formation are the clumps in WR (e.g. Moffat & Robert 1994) and O (e.g. Eversberg, Lepine & Moffat 1998) star winds. A test of the relative importance of these and the large-scale structures can come from imaging the newly formed dust in the IR. Marchenko, Moffat & Grosdidier (1998) observed large clumps of dust near WR 137 during its 1997 maximum, and Tuthill, Monnier & Danchi (1999), Monnier, Tuthill & Danchi (1999) and Tuthill et al. (2008) observed rotating 'pinwheel' dust structures around WR 104 (Ve2–45) and WR 98a (IRAS 17380–3031), characteristic of dust formed and emitted in a stream to one side of a binary system observed at a relatively low orbital inclination. The observation of non-thermal radio emission from the 'pinwheel' systems (Monnier et al. 2002a) provides further support for their binarity; but their stellar components have not been resolved, so it has not been possible to relate the positions of the stars and WCRs to that of the dust.

Such a comparison is now possible in the case of WR 140, whose dust emission was mapped by Monnier, Tuthill & Danchi (2002b, herafter MTD), and whose orbit is now fully determined in three dimensions. The RV orbital study by MM03 found a period, $P = 2899 \pm 1.3$ d, in excellent agreement with the IR photometric period, and an even greater eccentricity ($e = 0.881 \pm 0.005$) than those derived previously. From high-resolution imaging of the radio emission between phases 0.74 and 0.97, Dougherty et al. (2005) demonstrated that the WR 140 system rotates clockwise on the sky, and derived an orbital inclination, $i = 122^\circ \pm 5^\circ$, consistent with and more tightly constrained than that ($i = 50^\circ \pm 15^\circ$, equivalent to $i = 130^\circ \pm 15^\circ$) derived by MM03 from modelling the moving sub-peaks on the He I and C III line profiles. The binary itself was resolved by Monnier et al. (2004), who measured the stellar separation and position angle (PA) at phase 0.297. Using this and the inclination, Dougherty et al. determined the longitude of ascending node ($\Omega = 353^\circ \pm 3^\circ$), which, together with the argument of periastron ($\omega = 46\overset{\circ}{.}7 \pm 1\overset{\circ}{.}6$; MM03), completes the definition of the orbit.

The high-resolution near-IR images of WR 140 observed by MTD on 2001 June 12 and July 30 showed the dust to lie in several features of different size around the central star, and to be expanding with a proper motion of about 1.1 mas d^{-1}, but with no obvious relation to the orbit.

We therefore extended the imaging observations of WR 140 to study the evolution of the dust cloud and its relation to the colliding-wind structures inferred from the orbit and other observations. We also continued the infrared photometry reported in Paper I to confirm the periodicity determined from the 1970–1985 data and to improve the definition of the light curves around $\phi = 0.14$, which suggest enhanced dust formation, perhaps a secondary nucleation episode.

The two data sets are complementary: while the images show positions of the dust features and their angular expansion, the photometry allows the determination of the evolution of the 'average' temperature of the dust on account of the wide wavelength range and greater frequency of the observations. There is a caveat: the imaging data follow the 2001 periastron passage, whereas the photometric data come mostly from earlier periastron passages. The relation of the two data sets relies on the photometeric behaviour repeating periodically, which it appears to do (Section 3.4).

[1] Spectral types between O4–5 and O6 have been assigned to the primary in different studies. We re-examined the classification by measuring equivalent widths of the He I λ4471 and He II λ4542 lines, and derived the classification ratio (Conti & Alschuler 1971) $\log W' = \log W(4471) - \log W(4542) = -0.41 \pm 0.05$, which gives O5.5. This is later than the O4–5 derived from the optical spectrum by Lamontagne, Moffat & Seggewiss (1984) and from the UV spectrum in Paper I, but is consistent with the near equality of the He I (+He II) λ4025 and He II λ4200 lines (cf. Walborn & Fitzpatrick 1990). We adopt O5.

In Section 2, we report the infrared photometry in 1989–2001 and imaging observations in 2001–05. In Section 3, we use the light curves and images to describe the evolution of the dust cloud and use the positions and fluxes of the dust features to quantify the evolution. In Section 4, we attempt to model the dust images assuming the dust forms in the WCR rotating on the sky with the orbital motion and consider the influence of model parameters and some of the underlying assumptions on the fit. In Section 5, we discuss the results and the problems arising from the timing of the start and finish of the production of dust-forming plasma in the WCR and nucleation of the dust.

2 OBSERVATIONS

2.1 Photometry

The near-IR photometry (Table 1) was observed with a variety of telescopes: the United Kingdom Infrared Telescope (UKIRT), the Carlos Sánchez Telescope (TCS) of the Instituto Astrofísica de Canarias, the Telescopio InfraRosso del Gornergrat (TIRGO), the 2.1-m telescope of the Observatorio Astrónomico Nacional at San Pedro Mártir (SPM) and the University of Calgary 2-m Infrared Telescope (Calgary). Most of the observations were fitted in the gaps of other programmes, and the photometry is not expected to be as homogeneous as that from a single instrument or campaign. The uncertainties of the J, H and K magnitudes are typically 0.04 mag, while those of L' ($\lambda = 3.8\,\mu$m, $\Delta\lambda = 0.7\,\mu$m) and *nbM* ($\lambda = 4.63\,\mu$m, $\Delta\lambda = 0.17\,\mu$m) are less than 0.1 mag except where marked ':'. The *nbM* filter differs slightly from the M filter used for Paper I but the examination of the two data sets showed no systematic difference between M and *nbM* magnitudes, so we combined them. A comparison of the photometric standards used in common by UKIRT and the TCS revealed differences of 0.04, 0.03 and 0.04 mag in J, H and K, respectively, and these shifts were added to the TCS magnitudes in Table 1 for subsequent use. We made no adjustments to the other data sets. The final observation, although taken under hazy conditions, signalled the 2001 dust formation episode at $\phi = 0.02$.

The mid-IR data (Table 2) were observed with the bolometer photometer, UKT8, on UKIRT, or the Dual Infrared Camera, CID (Salas, Cruz-González & Tapia 2006), on the SPM 2.1-m telescope. The passbands of the intermediate bandwidth filters used for the CID observations differ slightly from the corresponding filters in UKT8, but the colour terms are expected to be smaller than the photometric uncertainties.

2.2 Imaging

The imaging observations (Table 3) were made with four different instruments: the Palomar High Angular Resolution Observer (PHARO) (Hayward et al. 2001) and AO (adaptive optics) system on the 5-m Hale telescope; the Isaac Newton Group Red Imaging Device (INGRID) (Packham et al. 2003) and NAOMI (Nasmythe Adaptive Optics for Multi-purpose Instrumentation) AO system on the 4.2-m William Herschel Telescope (WHT); the UKIRT 1–5 μm Imager Spectrometer (UIST) (Ramsay Howat et al. 2004) on the 3.8-m UKIRT and the Mid-infrared Imager/spectrometer (Michelle) (Glasse, Atad-Ettedgui & Harris 1997) on both UKIRT and the Gemini North telescope.

The PHARO observations were made on 2001 September 5, 2002 April 22 and 2002 July 25. The shortest frame time (1817 ms) available to the PHARO system required the use of a 1 per cent neutral-density filter in conjunction with the K filter. The pixel size was 25 mas and the position of WR 140 on the array was dithered between images. Prior to observation, the adaptive optics system was set up using the point spread function (PSF) standards, HD 203112 and HD 203856. Observations of WR 140 and the PSF standards were interspersed so that measurements were made at very similar airmasses. Images of the PSF standard, HD 203856, were used in further processing of each set of images using MEM2D

Table 1. New near-IR photometry of WR 140. The phases here and in Tables 2 and 3 were calculated using $P = 2900$ d and $T_0 = $ JD 2446 147 (1985.22). Observations made on two successive nights are replaced by their average and marked '*'.

Date	ϕ	J	H	K	L'	*nbM*	Telescope
1989.41	0.53	5.60	5.39	5.09	4.64		SPM
1989.65	0.56	5.60	5.42	5.10	4.70	4.32	UKIRT
1990.70	0.69	5.63	5.44	5.13		4.40	UKIRT
1991.41	0.78	5.57	5.36	5.04	4.87		SPM
1991.52	0.79	5.60	5.39	5.09	4.73	4.53	UKIRT
1991.79	0.83	5.59	5.39	5.08			TCS
1991.84	0.83	5.59	5.37	5.11	4.78	4.49	UKIRT
1992.29	0.89	5.59	5.39	5.04	4.77		TCS
1992.32	0.90	5.61	5.41	5.11	4.80	4.53	UKIRT
1992.32	0.90	5.64	5.43	5.09			TCS
1992.40	0.90	5.57	5.37	5.03	4.80		TCS
1992.55	0.92	5.61	5.40	5.04	4.84		TCS
1992.61	0.93	5.58	5.38	5.05	4.9:		TCS
1992.63	0.93	5.63	5.44	5.12	4.80	4.48	UKIRT
1992.67	0.94	5.61	5.41	5.08	4.9:		TCS
1992.82	0.96	5.63	5.39	5.04			TCS
1992.88	0.96	5.62	5.40	5.06	4.83		TCS
1993.03	0.98	5.58	5.36	5.00	4.94		TCS*
1993.32	0.02	5.38	4.55	3.54	2.25	1.91	UKIRT
1993.34	0.02		4.67	3.54			Calgary
1993.36	0.03		4.53	3.46			Calgary*
1993.40	0.03	5.40	4.71	3.66	2.27	1.97	UKIRT
1993.47	0.04	5.49	4.86	3.89	2.43	2.1:	UKIRT
1993.62	0.06	5.50	4.95	4.01	2.41		TCS
1993.66	0.06	5.56	5.03	4.16	2.48		TCS
1994.13	0.12	5.72	5.22	4.60	3.11		TCS
1994.20	0.13	5.63	5.26	4.52	2.9:		TCS
1994.28	0.14	5.74	5.26	4.60	3.05		TCS
1994.40	0.16	5.63	5.28	4.64	2.99		TCS
1994.70	0.19	5.57	5.28	4.72	3.6:		TCS
1994.93	0.22	5.61	5.38	4.87	3.96		TCS
1995.33	0.27	5.59	5.36	4.95	4.16		TCS
1995.57	0.30	5.57	5.38	4.96			TCS
1995.60	0.31	5.56	5.34	4.94			TCS
1995.62	0.31	5.64	5.36	5.01	4.20		TCS
1995.64	0.31	5.60	5.36	4.98			TCS
1995.89	0.34	5.52	5.35	4.98			TCS
1996.32	0.40	5.61	5.42	5.06			TCS
1996.39	0.41	5.62	5.39	5.03			TCS
1996.51	0.42	5.65	5.46	5.02			TCS
1996.59	0.43	5.59	5.36	5.02			TCS*
1996.61	0.43	5.62	5.40	5.02	4.39		TCS
1996.74	0.45	5.58	5.50	4.90	4.55		TIRGO
1997.58	0.56	5.62	5.40	5.05	4.7:		TCS
1997.63	0.56	5.67	5.46	5.09	4.56		TCS
1997.64	0.56	5.63	5.43	5.09	4.73		TCS
1997.65	0.57	5.66	5.42	5.08	4.57		TCS*
1998.72	0.70	5.63	5.42	5.06			TCS
1999.55	0.80	5.60	5.38	5.03			TCS
2001.25	0.02	5.1:	4.3:	3.2:	2.1:		TIRGO

© 2009 The Authors. Journal compilation © 2009 RAS, MNRAS **395,** 1749–1767

Table 2. New mid-infrared photometry of WR 140.

Date	ϕ	[8.75]	[12.5]	[19.5]	Tel
1990.66	0.69	3.40 ± 0.05	3.01 ± 0.10	2.0 ± 0.4	UKIRT
1992.63	0.93	3.91 ± 0.06	3.13 ± 0.11	2.6 ± 0.4	UKIRT
1993.50	0.04	1.68 ± 0.06	1.60 ± 0.08	1.8 ± 0.2	UKIRT
1994.32	0.15	1.64 ± 0.10	1.65 ± 0.05		UKIRT
1994.36	0.15			1.6 ± 0.1	UKIRT
2000.69	0.95	4.01 ± 0.20	3.26 ± 0.30		SPM

Table 3. Log of imaging observations of WR 140 including wavelengths and pixel sizes.

Telescope: instrument	Date	Phase	λobs (μm)	pixel (mas)
Hale: PHARO	2001.68	0.06	2.2	25.0
Hale: PHARO	2002.31	0.15	2.2	25.0
WHT: INGRID	2002.51	0.18	2.27	38.0
Hale: PHARO	2002.56	0.18	2.2	25.0
UKIRT: UIST	2002.89	0.23	3.6	60.6
UKIRT: UIST	2002.89	0.23	3.99	61.5
UKIRT: UIST	2003.42	0.29	3.6	60.6
UKIRT: UIST	2003.42	0.29	3.99	61.5
Gemini: Michelle	2003.86	0.35	7.9	100.5
Gemini: Michelle	2003.86	0.35	12.5	100.5
Gemini: Michelle	2003.96	0.36	7.9	100.5
Gemini: Michelle	2003.96	0.36	12.5	100.5
Gemini: Michelle	2003.96	0.36	18.5	100.5
UKIRT: Michelle	2004.25	0.40	10.5	210
UKIRT: UIST	2004.49	0.43	3.6	60.6
UKIRT: UIST	2004.49	0.43	3.99	61.1
UKIRT: UIST	2004.49	0.43	4.68	63.5
UKIRT: UIST	2004.71	0.46	3.99	61.1
UKIRT: UIST	2004.71	0.46	4.68	63.5
UKIRT: UIST	2005.52	0.56	3.99	61.5
UKIRT: UIST	2005.52	0.56	4.68	63.6

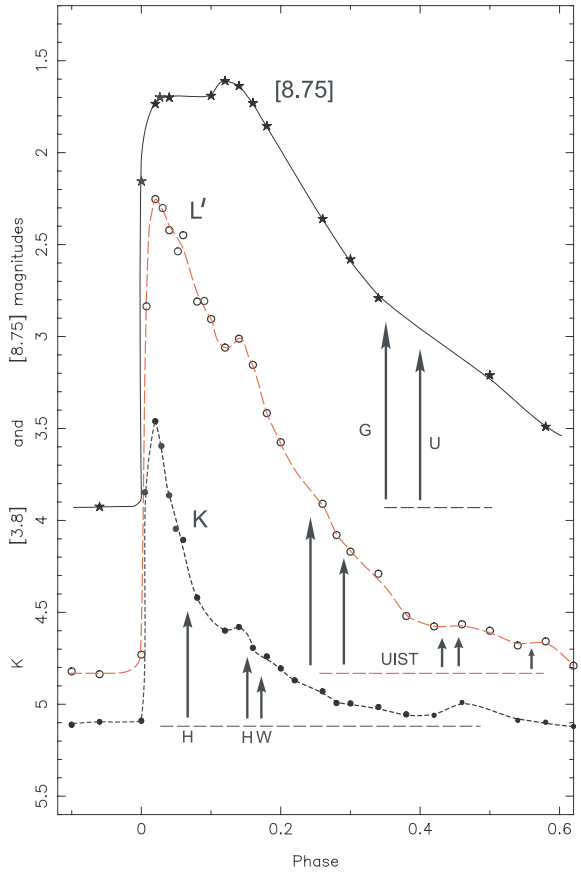

Figure 1. Infrared light curves of WR 140 at three wavelengths (8.75, 3.8 and 2.2 μm) showing the evolution of the dust emission. The phases of the imaging observations are marked on appropriate light curves. On the *K*-band curve, the phases of our PHARO *K*-band images are marked 'H', while that of our INGRID 2.27 μm observation are marked 'W' (the third PHARO observation at almost the same phase is omitted for clarity). The horizontal dashed line fitted to the pre-eruption photometry is assumed to give the underlying stellar flux, so that the contrast between dusty system and stellar fluxes at the times of the imaging observations is readily seen. Similarly, the phases of our UIST nbL', 3.99 μm and M' observations are marked on the L' (3.8 μm) light curve, and the Gemini North and UKIRT Michelle observations are marked 'G' and 'U' on the 8.75 μm light curve, with dashed lines again marking pre-eruption flux levels assumed indicative of the stellar fluxes.

routines in IRAF. Checks using images of HD 203112 for the PSF yielded consistent deconvolved images.

The INGRID observation was made on 2002 July 4 through the narrow-band *K*-cont filter ($\lambda = 2.27\,\mu$m, $\Delta\lambda = 0.03\,\mu$m). One hundred 3-s integrations of WR 140, dithered in a five-point pattern on the chip, were combined using Starlink CCDPACK routines. These data were taken in two runs, separated by sets of 10-s integrations of the PSF star HD 203856. Initially, the WR 140 data in the two runs were reduced separately to allow a comparison of the two combined images. Both showed very similar structures, giving confidence that they were real. The images were then reconstructed with the MEM2D maximum entropy routine using the combined images of HD 203856 for the PSF. The reconstructed image is shown later in Fig. 3. The central wavelengths of the *K*- and *K*-cont filters are close enough for us to treat the PHARO and INGRID images together, and we will refer to them as '2 μm images'.

From the *K*-band light curve (Fig. 1), it can be seen that the contrast, the difference between the total (dust+star) and stellar emission (assumed to be equal to the pre-outburst emission), fell from 0.85 to 0.35 mag during our sequence of 2 μm imaging observations.

The UIST observations were all made in the UKIRT Service Observing programme. Image stabilization was provided by an active tip-tilt secondary. The observations were taken by nodding the telescope to four points on the array, subtracting adjacent frames and adding the pairs. The PSF standards were observed on the same regions of the array as WR 140 and with the same jitter pattern. Individual integration times were typically 4 s in nbL' and [3.99] and 0.4 s in M', repeated to give total integration times of, typically, 400 s on WR 140. Preliminary reduction of the data was done using ORACDR, the pipeline data reduction at the telescope. Final reduction, involving matching the centroids, averaging the frames and MEM2D reconstruction, was then done using the Starlink packages KAPPA and CCDPACK.

During the campaign, we observed through progressively longer wavelength filters as the dust cooled and the contrast at the shorter wavelengths fell. On 2002 November 20 and 2003 June 4, we used the narrow-band nbL' ($\lambda = 3.6\,\mu$m) and [3.99] ($\lambda = 3.99\,\mu$m) filters; on 2004 June 27, we added the M' ($\lambda = 4.68\,\mu$m) filter, which is similar to the *nbM* filter used for the photometry. As the dust cooled further, we dropped the nbL' filter for the 2004 September 18 and 2005 July 21 observations. The longer wavelengths and

slightly smaller aperture of the telescope meant that these images had about half the spatial resolution of our 2 μm images observed in 2002. From the comparison stars, we measured PSFs of 0.36 arcsec [full width at half maximum (FWHM)] at 3.99 μm, compared with 0.19 arcsec (FWHM) on the 2.27 μm INGRID images.

The PSF standard for UIST observations in 2004–05 was the UKIRT photometric standard HD 201941, allowing calibration of the images. This yielded $M' = 4.11$, 4.16 and 4.34 at phases 0.43, 0.46 and 0.56, respectively, in excellent agreement with the *M*/*nbM* light curve.

Images in the mid-IR were observed using Michelle on Gemini North on 2003 November 9 and December 15. The data were acquired in a regular chop-nod pattern, with an on-chip 15 arcsec E–W chop throw and N–S nodding. For combination of images coming from multiple exposures, we used only the chopped images taken under active guidance with a peripheral wavefront sensor. The images have resolutions (0.50 arcsec at 7.9 μm and 0.59 arcsec at 12.5 μm, from observations of the standard star PSFs) somewhat lower than those of the UIST images because the longer wavelengths outweigh the advantages of the larger aperture of Gemini.

Another mid-IR observation with Michelle, this time on UKIRT, was made on 2004 March 31 in the UKIRT Service Observing Programme. The secondary was chopped 15 arcsec N–S and the telescope nodded 15 arcsec E–W. The final image was formed by matching the centroids of the four stellar images and averaging them. The object and the standard (BS 7525) were observed on the same region of the array with the same nod and chop offsets and exposure times. Preliminary reduction of these data used ORACDR, and final reduction, involving matching the centroids, averaging the frames and MEM2D reconstruction, used the Starlink packages KAPPA and CCDPACK. The derived magnitude, $N = 2.9 \pm 0.2$, of the (star+dust) system at phase 0.40 is consistent with the [8.75]- and [12.5]-band light curves.

3 EVOLUTION OF THE DUST EMISSION AND EXPANSION OF THE CLOUD

3.1 Photometry and properties of the dust grains

The new data strengthen the determination of the pre-eruption SED, for which we adopt $H = 5.43$, $K = 5.12$, $L' = 4.82$, $M/nbM = 4.53$, $[8.75] = 3.95$, $[12.5] = 3.2$ and $[19.5] = 2.8$. They also define the stellar SED, i.e. neglecting any contribution from dust made in the 1993 and earlier eruptions (see below). These are used as a baseline for modelling the post-eruption SEDs and, in Section 3.5, for calibrating the images, assuming the stellar flux not to vary over the period of the imaging observations – a view supported by the optical monitoring (MM03), which shows long-term stability between periastron passages.

A comparison of the new data with those in Paper I and Williams et al. (1978) shows that the behaviour followed that observed from previous periastron passages and allows the re-examination of the photometric period. The Lafler–Kinman period searches on the data in the fading branches of the H, K and L' light curves give periods of 2905 ± 8, 2900 ± 4 and 2905 ± 10 d, respectively, slightly longer than the 2900 ± 10 d found in Paper I and the RV period (2899 ± 1.3 d; MM03). We adopt a weighted mean period of 2900 d. Unfortunately, we were not able to observe the much steeper rising branches of the light curve in either 1993 or 2001 which, with the 1985 rise, would give a significantly more precise period.

Using this period and MM03's T_0, we produced light curves gridded to intervals of 0.02 P (0.01 P for $0 < \phi < 0.1$) at three

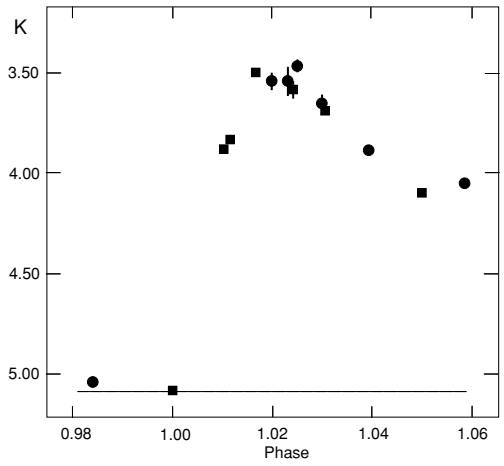

Figure 2. Light curve of WR 140 near periastron in K with observations from the 1985 (squares) and 1993 (circles) maxima. The horizontal line represents the level of the stellar wind emission.

representative wavelengths (Fig. 1) to illustrate the level of dust emission relative to that of the star at the phases of the imaging observations, and summarize the evolution of the dust emission. To show the beginning and duration of the condensation of new grains, we show (Fig. 2) the K-band light curve near periastron based on individual magnitudes observed during the 1985 and 1993 events. Phased light curves in more filters, albeit based on fewer data, were given in Paper I.

The light curves track the evolution of the dust emission integrated over all the individual features comprising different masses of dust at different temperatures. An average dust temperature, $\langle T_g \rangle$, can be determined for the dust at each phase by fitting the multi-wavelength photometry with optically thin emission by carbon grains after correcting for interstellar reddening and subtracting the stellar SED, as in Paper I. Here we adopted $A_V = 2.9$ (Morris et al. 1993) and absorption coefficients of the 'ACAR' amorphous carbon grains prepared in an inert (Argon) atmosphere in the laboratory by Colangeli et al. (1995). Cross-sections were calculated using the optical properties for this sample given by Zubko et al. (1996). Model SEDs calculated using the 'ACAR' data gave a better fit to broad features in the 5.5–6.5 μm *Infrared Space Observatory* spectra of dust-making WC8–10 stars (Williams, van der Hucht & Morris 1998) than those based on the 'ACH2' grains produced by Colangeli et al. in a hydrogen atmosphere – as one might expect for grains formed in hydrogen-poor WC stellar winds. The temperature, T_g, of a grain is determined primarily by its radiative equilibrium in the stellar radiation field at distances r_O and r_W from the O5 and WC7 stars:

$$4\overline{Q}_a(a, T_g)T_g^4 = \frac{\overline{Q}_a(a, T_O)T_O^4}{(r_O/R_O)^2} + \frac{\overline{Q}_a(a, T_W)T_W^4}{(r_W/R_W)^2},$$

where $\overline{Q}_a(a, T)$ are the Planck mean absorption cross-sections appropriate to the grain or stellar temperature for grains of radius a, and the factor of 4 is for spherical grains. The ACAR grains have $\overline{Q}_a(a, T_g) \propto T_g^{1.2}$ in the relevant temperature range, so the radiative-equilibrium grain temperature falls off with distance as $T_g \propto r^{-0.38}$ for constant grain size and stellar luminosity. We assume the distance between the two stars is much smaller than that of the dust to either, and use r for r_O and r_W. We can derive distances corresponding to the average temperatures, allowing us to track the movement of the dust away from the stars, especially in the early phases when the dust emission has not been imaged. The dust inherits the

velocity of the compressed wind from which it condenses and will then be accelerated by radiation pressure so, in the absence of any other effect, newly made dust will cool as it moves from the stars, and its emission will fade.

Fits to the H to [19.5] and H to [12.5] data at phases 0.01 and 0.02 gave $\langle T_g \rangle \simeq 1100$ K and dust masses $M_g = 2 \times 10^{-8}$ and $3 \times 10^{-8}\,M_\odot$. The approximate constancy of $\langle T_g \rangle$ and therefore the radiative-equilibrium r at these phases while the dust mass rose can be interpreted as continued condensation of new dust at a fixed distance from the stars. This is the nucleation radius, the closest to the stars that grains can survive sublimation. At $\phi = 0.00$, we have only $JHKL'$ data, and the fit to them gives $\langle T_g \rangle \simeq 1200$ K and $M_g = 2 \times 10^{-10}\,M_\odot$ or, fixing the temperature at 1100 K, $M_g = 3 \times 10^{-10}\,M_\odot$, so it is evident that dust formation had just begun at periastron. This is supported by the individual *JHK* observations, which show (e.g. Fig. 2) no significant excess over wind emission at phases $\phi = 0.844$ and 0.999 and a broad maximum around $\phi = 0.025$. By $\phi = 0.03$, the $JHKL'$ magnitudes and temperature were falling, indicating that no new dust was condensing to replenish the dust carried away with the wind. From $\phi = 0.03$ to 0.12, the near-IR flux fell while the mid-IR flux rose to maximum. The model fits to the SEDs show that the dust mass doubled to $6 \times 10^{-8}\,M_\odot$ while $\langle T_g \rangle$ fell to 800 K. This suggests that the increase of dust mass was caused by the growth of the recently formed grains at their equilibrium temperature rather than by the condensation of fresh grains at $T_g \simeq 1100$ K. Zubko (1998) has shown that carbon grains in WC9 stellar winds grow to $a \sim 100$ Å by implantation of impinging carbon ions as they move through the wind after acceleration by radiation pressure. Evidence for larger grains made in WR 140 comes from eclipses observed in the optical light curves between phases 0.020 and 0.055, from which MM03 derived a typical size of 0.069 μm (690Å) for dust grains in our line of sight to the star.

The K and L' light curves show an inflexion at $\phi = 0.14$, suggesting a short-lived increase in dust emission. The *UBV* photometry (MM03) does not show brightening at this time, so we ascribe the extra emission to an increase of dust formation rather than increased radiative heating of the dust. The H photometry does not show any interruption in its fading at this phase, suggesting that the brightening at K and L' does not come from the condensation of new, hot dust but from a temporary increase in grain growth rate.

After $\phi = 0.14$, the fading continues at all wavelengths and the dust cools as expected. The total mass, however, falls from its maximum of $6.5 \times 10^{-8}\,M_\odot$ to less than $2 \times 10^{-8}\,M_\odot$ at phase 0.56. This may be an artefact arising from our use of isothermal dust models, but a similar effect was observed when modelling the then available IR photometry with radially extended dust parcels having an appropriate range of T_g in Paper I, so we believe the effect to be real. It suggests that, as grains move through the wind, the rate of destruction by thermal sputtering eventually overtakes that of growth by implantation of carbon ions (cf. Zubko 1998) and grains are destroyed.

The temperatures and dust masses derived here differ from those in Paper I because we used different optical constants for the grains. We note that the condensation temperature, 1100 K, found here is lower than those found from modelling WC9 SEDs by Zubko (1998) or modelling the dust pinwheel about WR 104 by Harries et al. (2004) using the same 'ACAR' dust analogue and optical coefficients. This suggests that either the dust formed by WR 140 has different optical properties from that made by the WC9 stars or a difference in conditions, e.g. stronger radiation field or faster stellar winds, affects the condensation.

We estimate the nucleation radius, the distance from the stars corresponding to the condensation temperature, by modelling the heating of the dust. Because the UV-optical spectra of hot stars are not Planckian, we calculated model atmosphere analogues of Planck mean cross-sections $\overline{Q}_a(a, T_O)$ and $\overline{Q}_a(a, T_W)$ using the 35 kK WM-Basic O-star model fluxes tabulated by Smith, Norris & Crowther (2002) for the O5 star, and their 70 kK CMFGEN WC model fluxes for the WC7 component, and absorption coefficients for small ACAR grains. The temperature chosen for the O-star model comes from the calibration of WM-Basic models by Garcia & Bianca (2004) and our revised type of O5. The luminosity and radius of the O5 star were determined by fitting the WM-Basic flux to its de-reddened v magnitude and the distance of 1850 pc determined by Dougherty et al. (2005), giving $R_O = 26 R_\odot$ and $\log(L/L_\odot) = 5.93$. The luminosity is lower than that [$\log(L/L_\odot) = 6.18$] adopted by Pittard & Dougherty (2006) and close to the typical values (5.6–5.93) given for O5 I–III stars by Repolust, Puls & Herrero (2004). We retained the Pittard & Dougherty luminosity of the WC7 star [$\log(L/L_\odot) = 5.5$]; it provides about one-quarter of the radiation heating the grains.

The equilibrium distance corresponding to $T_g = 1100$ K for small (10-50 Å) grains is $r \simeq 630$ au. For a distance of 1850 pc (Dougherty et al. 2005), this would subtend 340 mas, significantly greater than the distances (54–220 mas) at which MTD observed condensations in 2001 June ($\phi = 0.039$). Larger grains are relatively more efficient at cooling, e.g. 0.1 μm grains would attain $T_g = 1100$ K at $r \simeq 235$ au, but large grains have to start as condensation nuclei, so this cannot account for the discrepancy. Nor is it likely to be an inclination effect: although the inclination angles of the trajectories of these dust clouds are not known, a comparison of their projected velocities (MTD and Section 3.3) with the wind velocities suggests low inclinations. Nor is it a consequence of the adopted distance to WR 140: if WR 140 were closer, the stars would be less luminous, their radii smaller, the radiative equilibrium distance to the dust smaller in proportion, but the angular equilibrium distance would be unchanged. The compressed winds within which the grains condense may provide some shielding from the stellar radiation, but only a difference in dust properties can account for most of the discrepancy.

A comparison of several laboratory analogues of cosmic amorphous carbon grains by Andersen, Loidl & Höfner (1999) shows that their absorption efficiencies have fairly similar wavelength dependencies ($\kappa \propto \lambda^{-1.1}$) in the IR, but absolute values and ratios of ultraviolet-to-IR coefficients ranging by a factor of ∼5. Consequently, while the grain temperatures derived from fitting IR SEDs are relatively insensitive to the choice of grain sample, the absolute dust masses and the distances derived from grain temperatures through equilibrium in hot star radiation *do* depend on the choice of sample.[2]

We suggest that the dust formed by WR 140 has a lower ratio of ultraviolet-to-IR opacities than the 'ACAR' sample. For a rough approximation, we introduce a scaling factor to the UV opacity scale so as to produce an equilibrium temperature at a typical distance (150 au) of a condensation in MTD's 2001 June image equal to that determined from the SED, $\langle T_g \rangle = 980$K, at that phase ($\phi = 0.039$),

[2] Planck mean cross-sections of the different samples at typical grain temperatures have similar temperature dependence, so the $r^{-0.38}$ rate at which T_g falls off with distance is also fairly insensitive to the choice of sample, as are the *relative* masses of dust determined from SEDs observed at different phases.

using a grain size of 100 Å to allow for grain growth. With this scaling, the equilibrium distance for small grains would then be a more plausible 125 au.

We continue by applying the same scalefactor to calculate the Planck mean cross-sections for radiation pressure, $\overline{Q}_{\rm pr}(a, T_\star)$, and hence the acceleration of the grains:

$$\ddot{r} = \frac{3\sigma}{4acs_{\rm g}}\left[\frac{\overline{Q}_{\rm pr}(a, T_{\rm O})T_{\rm O}^4}{(r_{\rm O}/R_{\rm O})^2} + \frac{\overline{Q}_{\rm pr}(a, T_{\rm W})T_{\rm W}^4}{(r_{\rm W}/R_{\rm W})^2}\right].$$

Assuming a bulk density $s_{\rm g} = 2\,{\rm g\,cm^{-3}}$ for the grain material, the acceleration at $r = 125$ au would be about 33 km s^{-1} per day for a 10 Å grain and not much less, 30 km s^{-1} per day, for a 100 Å grain. After only a few days, the grains would have significant drift velocities, u, relative to the material in which they formed. The principal limitation on the acceleration is supersonic drag, which is approximately proportional to u^2 and the local density, $\rho(r)$. As the grains accelerate, the drag increases until it balances the radiation pressure. If the grains are moving through a wind having $\rho(r) \propto r^{-2}$, both forces are proportional to r^{-2}, and the grains will take up a terminal drift velocity relative to the wind. The imaging observations allow us to estimate this velocity (Section 3.3).

3.2 The images and expansion of the dust cloud

Our images of WR 140 in Figs 3–5 do not resolve the binary itself, which we will refer to as the star here. To allow easy intercomparison, the 2 μm images and the first sets of UIST images (Fig. 3) have been plotted on a common scale (2.4 arcsec^2), and most of the subsequent images (Fig. 4) on a larger (4 arcsec^2) common scale to accommodate the expanded dust cloud.

The first PHARO observation (Fig. 3) was made five weeks after the 2001 July 30 Keck observations by MTD and Tuthill et al. (2003). It shows extended emission to the south and east of the central star, consistent with the Keck images, but does not resolve the dust emission features.

By the time of the second PHARO observation in 2002 April, the cloud had expanded sufficiently for us to resolve some of the dust features previously observed in the Keck images. Following MTD, we identified prominent dust-emission peaks and measured their positions relative to the star. The PAs (E of N) and projected distances (ξ) are given in Table 4. At the scale of these images, uncertainties of ± 1 pixel in the measured positions yield uncertainties of 5° in PA and 30 mas in ξ. The principal feature apparent in the images here is a 'bar' of emission (marked 'bar' in Fig. 3) to the south of the central star (marked 'S'), and extending E–W. The 'bar' is evident in the 2.26 μm Keck image of 2001 July (Tuthill et al. 2003), but only the peaks at the two ends are seen in their 3.08 μm image observed on the same date. We label the emission peaks at the E and W ends of the 'bar' as 'C0' and 'C1' in all our images. A comparison of the morphology of the 'bar' structure in the Keck images and those presented here suggests a connection between 'C1' and their 'Feature C' but the PAs differ by about 12°, arguing against their being the same physical entity in radial expansion. We estimated the PA of a concentration having a PA similar to that of 'C1' in the published 2001 July 2.21 μm Keck image and give its position in Table 4.

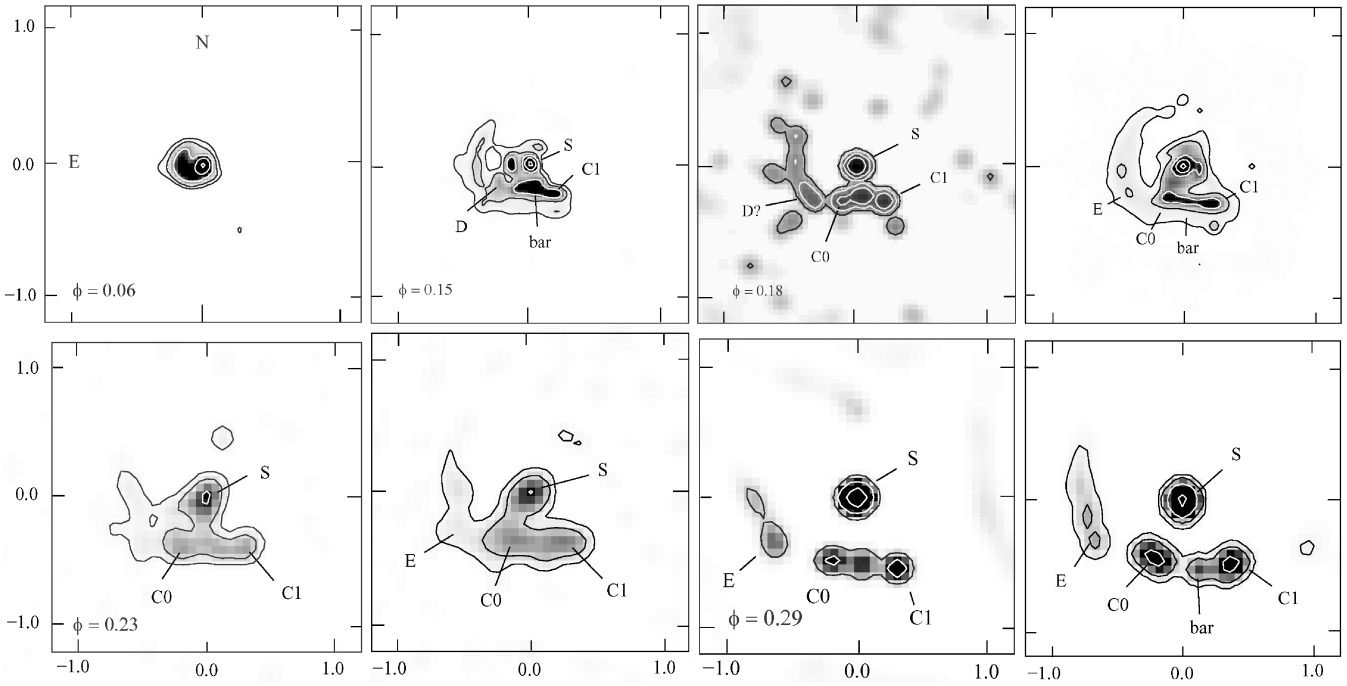

Figure 3. Images presented at the same scale (2.4 arcsec^2) and orientation to show evolution of the dust emission from $\phi = 0.06$ to 0.29. Superimposed on the grey-scale images are contours drawn at the same, equal logarithmic flux intervals (0.8 dex, 2 mag). The images are centred on the star ('S'), and the positions of the dust emission features 'C1', etc., are given in Table 4. Top (left–right): 2 μm images observed on 2001 September 5 ($\phi = 0.06$) and 2002 April 22 ($\phi = 0.15$) with the PHARO/AO system on the Hale telescope. The third and fourth images were observed within three weeks of each other at $\phi = 0.18$, on 2002 July 4 with the NAOMI/INGRID system on the WHT and on July 22 with the PHARO/AO system. The PSF was measured from the comparison star observations to be 0.19 arcsec (FWHM). Bottom (left–right) pairs of images through the nbL' and [3.99] filters observed with UIST on UKIRT on 2002 November 20 ($\phi = 0.23$) and 2003 June 4 ($\phi = 0.29$). Owing to the longer wavelengths of observations, their resolution is about half that of the 2 μm images, with typical PSFs of 0.36 arcsec (FWHM) measured from the comparison stars.

© 2009 The Authors. Journal compilation © 2009 RAS, MNRAS **395,** 1749–1767

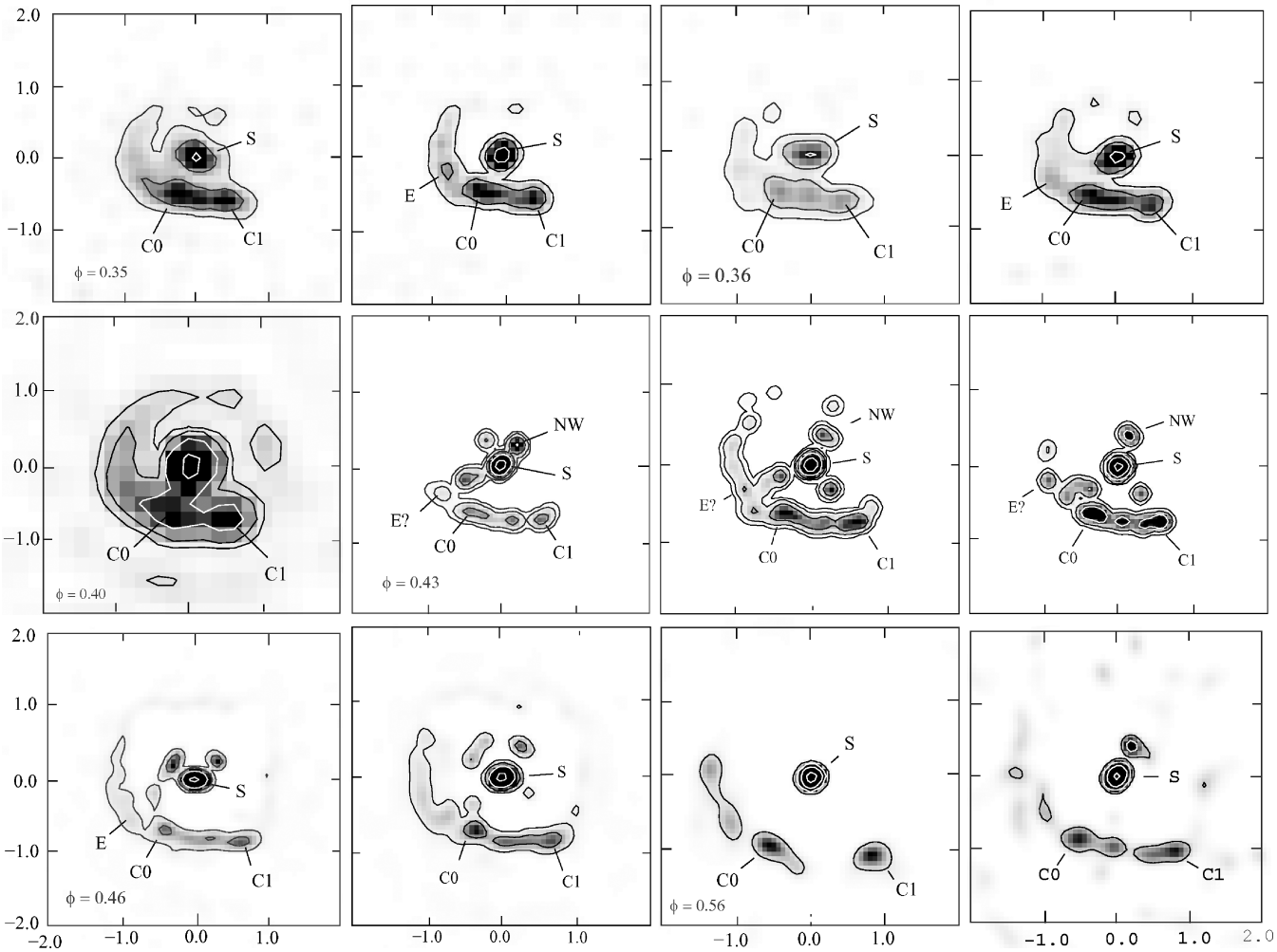

Figure 4. Images presented at a larger scale (4 arcsec^2) to show later evolution of the dust emission ($\phi = 0.35$–0.56); the orientations and contour intervals are as in Fig. 3. Top row (left–right): pairs of images observed with Michelle on Gemini North through the narrow-band 7.9 and 12.5 μm filters on 2003 November 9 ($\phi = 0.35$) and December 15 ($\phi = 0.36$). The PSFs of the comparison stars were measured to be 0.50 arcsec at 7.9 μm and 0.59 arcsec at 12.5 μm, slightly larger than those of the UKIRT/UIST nbL' and [3.99] images as the longer wavelengths are partly compensated for by the larger aperture of Gemini. Middle row (left–right): image at 10.5 μm observed with Michelle on UKIRT on 2004 March 31 ($\phi = 0.40$), which has the lowest resolution (PSF 0.8 arcsec FWHM) on account of the wavelength and telescope aperture, followed by three images observed with UIST on UKIRT on 2004 June 27 ($\phi = 0.43$) through the nbL', [3.99] and M' filters. We are not sure that we have measured 'E' in these and find compact features considered to be artefacts (e.g. 'NW'; see text) nearer the star. These appear in the subsequent images below, and do not share the movement of the dust features away from the star. Bottom row (left–right): pairs of images observed with UKIRT/UIST through the [3.99] and M' filters on 2004 September 25 ($\phi = 0.46$) and 2005 July 21 ($\phi = 0.56$).

Our April PHARO image shows other structures seen in the Keck images, notably the 'arm' to the east, which lies further from the star than the 'bar', and an intermediate concentration which we tentatively identify with MTD's 'Feature D' on the basis of its PA (Table 4). We measured the K-band flux of the whole structure using a 0.9 arcsec software aperture and that of the star alone with a 0.18 arcsec aperture, and determined a difference of 0.6 mag. This difference is consistent with the K-band light curve (Fig. 1) at the time of observation.

The next two images in Fig. 3 come from observations made within three weeks of each other (July 4 and July 25) using two different instruments (INGRID and PHARO) and reduced independently using different software suites. Assuming there was no significant change in the morphology of the dust emission (apart from expansion of the cloud) during this time, a comparison of the images provides an excellent external check on the veracity of the structures revealed in the maximum-entropy reconstructions. Again, the most conspicuous feature is the E–W 'bar' to the S, at the ends of which we have measured the positions of 'C0' and 'C1'. The PAs (Table 4) agree well with those observed in the April image, and the radial distances show continued expansion of the dust structure. We measured the intensity profiles of 'C1', finding it to be extended E–W, but unresolved N–S, consistent with its being a concentration in a thin, elongated structure. Although we refer to dust emission features as 'concentrations', we are aware that these are not necessarily physical clumps. The dust is optically thin in the IR (Paper I), and we expect it to form extended, hollow structures owing to its origin in a hollow, thin WCR (cf. Section 4.2), so that the brightest emission could be coming from the limb-brightened edges of the structures.

Both the INGRID and PHARO images show the 'arms' of emission to the east of the star, but somewhat differing in form: that in the PHARO image has the same angular extent (PA 15°–125°) as in the Keck images, while that in the INGRID image is truncated, perhaps

Table 4. Position angles (PA, deg. east of north) and projected distances (ξ, mas), relative to the central star, of dust 'knots' identified in the IR images. The positions from the Keck observations come from MTD except those marked (*), which were made by us from their 2.21 μm image or the 3.08 μm image in Tuthill et al. (2003).

Tel: Inst	Date	Phase	λobs	knot C1		knot C0		knot D		knot E	
			(μm)	(PA)	(ξ)	(PA)	(ξ)	(PA)	(ξ)	(PA)	(ξ)
Keck (MTD)	2001.45	0.04	2.21	231	54			134	77	113	110
Keck (MTD)	2001.58	0.06	2.21	227	76	*154	*64	136	125	113	172
Keck (Tuthill et al.)	2001.58	0.06	3.08	*229	*91			*133	*99	*114	*175
Hale: PHARO	2002.31	0.15	2.2	216	278	161	204				
WHT: INGRID	2002.51	0.18	2.27	219	343	157	290	124	419		
Hale: PHARO	2002.56	0.18	2.2	217	352	157	261			115	467
UKIRT: UIST	2002.89	0.23	3.6	217	498	163	330				
UKIRT: UIST	2002.89	0.23	3.99	216	460	168	360			115	577
UKIRT: UIST	2003.42	0.29	3.6	209	626	158	526			118	729
UKIRT: UIST	2003.42	0.29	3.99	217	601	156	491			119	759
Gemini: Michelle	2003.86	0.35	7.9	214	714	153	553			112	812
Gemini: Michelle	2003.86	0.35	12.5	213	736	157	603			107	842
Gemini: Michelle	2003.96	0.36	7.9	214	755	141	654			102	976
Gemini: Michelle	2003.96	0.36	12.5	213	780	145	632			110	960
UKIRT: Michelle	2004.25	0.40	10.5	215	874	162	684				
UKIRT: UIST	2004.49	0.43	3.6	216	926	148	766				
UKIRT: UIST	2004.49	0.43	3.99	219	986	149	749				
UKIRT: UIST	2004.49	0.43	4.68	218	966	157	727				
UKIRT: UIST	2004.71	0.46	3.99	216	1055	149	781				
UKIRT: UIST	2004.71	0.46	4.68	218	1072	154	778				
UKIRT: UIST	2005.52	0.56	3.99	218	1363	149	1079				
UKIRT: UIST	2005.52	0.56	4.68	218	1326	150	1013				

in the image deconvolution. We measured an emission peak at a PA close to MTD's Feature 'E' in the PHARO image and tentatively one about 10° in PA from their 'Feature D' in the INGRID image (Table 4). We observe extended emission near MTD's 'Feature A' at the N ends of the 'arms' but not their 'Feature B' to the NW of the star.

The UIST observations were made at longer wavelengths, initially 3.6 and 3.99 μm, where the contrast between dust and stellar emission was expected to be greater (cf. Fig. 1). The 2002–03 UIST images in Fig. 3 all show the 'bar' to the south which, in the 2003 images, appears to be resolved into three components, reminiscent of the INGRID 2 μm image. These structures, however, may be a consequence of the reconstruction of faint diffuse emission in the presence of noise, which can produce spurious concentrations. The N–S image profiles of 'C1' have half-widths equal to that of the star, so the 'bar' is unresolved in this direction. These images also show the 'arm' of emission to the east, more evidently in the 3.99 μm images, in which we identify knot 'E' but not much emission to the N of it, let alone anything corresponding to MTD's 'Feature A' at the N end.

In the top panel of Fig. 4, we present the mid-infrared images observed with Michelle on Gemini North. The structures of the dust clouds look very similar to those observed earlier, and we can identify and measure most of the same emission features. Their positions are included in Table 4. The PAs of 'E' show some scatter as we measure different points along the 'arm' owing to its relative faintness and the fact that we are measuring a bright part of extended emission, but the radial distances are more certain and show continued uniform expansion of the dust cloud.

The December 12.5 μm image shows faint emission further south of the cloud which we identify as a remnant of the dust formed at the time of the previous (1993) periastron passage. This image is shown at lower scale in Fig. 5, both with contours as in the other figures and in grey-scale only, combined with the November image to bring out the fainter emission. In the former, we have marked two features 'F' and 'G' which have PAs (150° and 215°) very close to the mean PAs of knots 'C0' (154°) and 'C1' (216°) from all our observations (cf. Table 4). If 'F' and 'G' had travelled from the star since the 1993 periastron passage, their average proper motions over the intervening 10.6 yr would have been 235 and 319 mas yr^{-1}, respectively, in good agreement with the average proper motions of 'C0' and 'C1' (244 ± 9 and 326 ± 7 mas yr^{-1}) determined from our 2002–05 observations (Table 5; Section 3.3).

The continued linear expansion of the dust cloud points to expansion into a low-density circumstellar environment, essentially the cavity blown by the stellar winds of the two components during their main-sequence lifetimes and observed as a minimum in H I emission by Arnal (2001). The cavity has a diameter of 110 arcmin and is also seen as a ragged shell at *IRAS* wavelengths (Marston 1996). Its dynamical age (>1 million yr) suggests that it was formed during the earlier O-star phase of the WC7 star.

In 2004, we re-observed WR 140 in the mid-IR using Michelle, but this time on UKIRT. The resolution of the image (Fig. 4) is lower than those of the Gemini observations owing to the smaller aperture of the telescope, but the principal dust features are still observable and we give the positions of 'C1' and 'C0' in Table 4. The PA of 'C0' differs by 8° from the average PA (154°) for this feature – which equates to half a relatively large (210 mas) pixel in this instrument on UKIRT. The PA of 'C1' agrees with the average within a small fraction of a pixel, and the radial distances of both features fit the linear expansion (Fig. 6, Table 5) to within a quarter pixel.

The other three images in the middle panel of Fig. 4 were observed with UIST on 2004 June 27, when the contrast between stellar and dust emission was much lower (cf. the L'-band light curve in Fig. 1). The principal dust feature, the 'bar' including 'C0' and

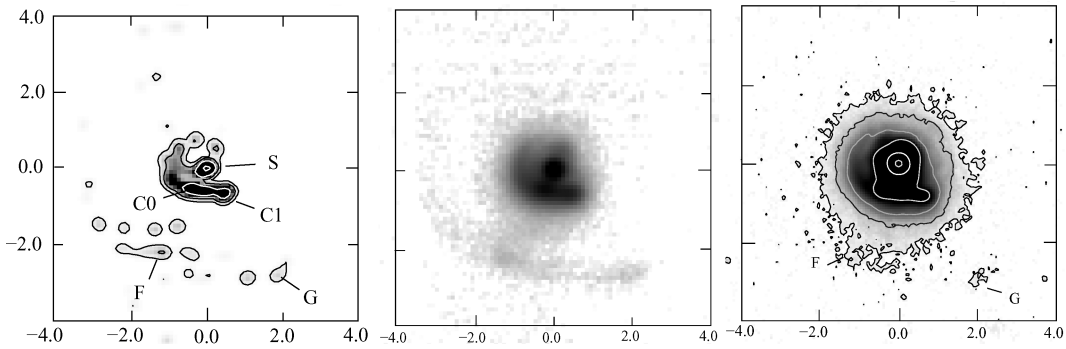

Figure 5. Images at a larger scale (8 arcsec^2) to show the faint emission features believed to be the remnants of the dust formed in the 1993 episode, including 'F' and 'G', which have PAs very close to those of 'C0' and 'C1' and distances consistent with their being one period older (Section 3.2). Left: the 2003 December 12.5 μm image with lowest contour level (3.7σ sky) well below that (20 σ sky) in the corresponding image in Fig. 4. Centre: the November and December 12.5 μm images combined, and plotted with an intensity scale chosen to emphasize the faint emission features. Right: the unreconstructed 2004 September 25 M' image at an intensity scale chosen to bring out the fainter emission, including 'F' on the outskirts of the central emission the equivalent of 'C0' formed in the 1993 dust formation episode.

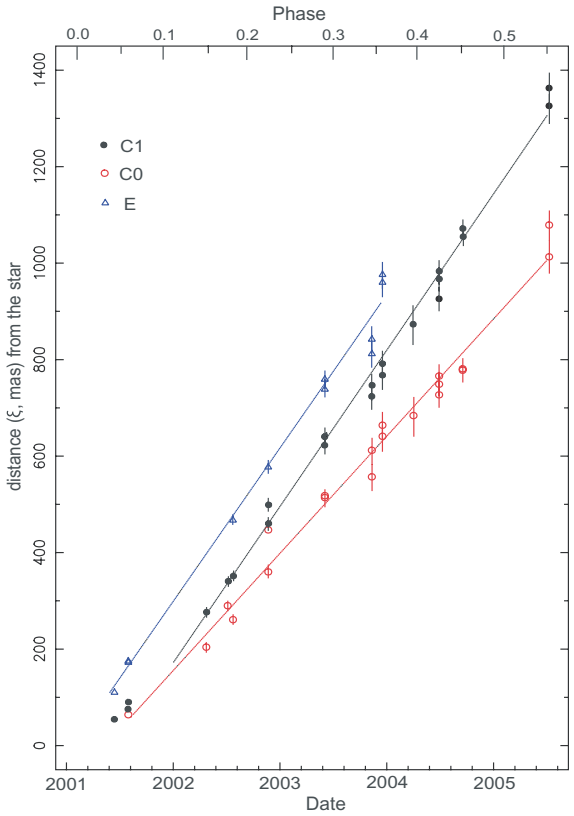

Figure 6. Angular distances (ξ) of prominent dust emission features 'C1', 'C0' and 'E' plotted against date (Table 4). The straight lines are linear fits to our data and the Keck observations of 'Feature E', which we identify with our 'E'.

'C1', is clearly present (and seen in the raw images). We also observe compact features nearer the star, one to the NW (marked 'NW') at all three wavelengths. The M' UIST images observed in 2004 September and 2005 July (bottom panel of Fig. 4) also show compact features to the NW, but the insignificance of the proper motion from these three observations, 17 ± 28 mas yr^{-1}, shows that 'NW' is *not* a dust feature moving from the star or a re-appearance of MTD's 'Feature B', which had a similar PA. The [3.99] and M' 2004 June images also show a concentration at the same PA as 'C1' but closer to the star, but this is not seen in the later images. The radial distances of all these concentrations show a strong correlation with the wavelength of the observation, and the average distance is proportional to wavelength, being about 15 per cent greater than the radius of the first Airy ring (1.635 arcsec λ/D), so we consider them to be instrumental artefacts. This is a characteristic bias of MEM-deconvolved images of a point source embedded in extended emission (Monnier 2003) and are seen only in our later images because of the relative faintness of the dust emission features.

The positions of 'C1' and 'C0' are included in Table 4, and confirm the continued motion of the southern dust feature(s) (Fig. 6). The 'arm' is seen in the 3.99 μm images but is getting lost in the noise, and it is not possible to identify 'E' with enough confidence to track its position. The 2004 September and 2005 July images follow the same pattern: confirmation of the expansion of the southern dust-emission peaks (Table 4, Fig. 6) and the presence of the eastern 'arm', but no concentration corresponding to 'E'.

We examined the UIST images for traces of the dust formed in the 1993 episode, such as those seen in the 12.5 μm image. Only the M' image observed on 2004 September 18, when the water vapour content above the telescope was very low, shows emission near the expected position (Fig. 5, a direct image without MEM-reconstruction to avoid possible introduction of artefacts). We observed a faint patch at PA 216°, close to that of 'C1', located 3568 mas from the star. If this is dust formed in the 1993 episode, the mean proper motion over the intervening 1.46 P would be 308 mas yr^{-1}, smaller than the 319 mas yr^{-1} for the corresponding feature in the 12.5 μm image observed in 2003 and the average proper motion of 'C1' (326 ± 7 mas yr^{-1}) from our 2002–05 observations (Table 5), suggesting that the dust may be slowing down. The outskirts of the central image show extended emission to the SW, which we have marked 'F', at PA = 155°, at a distance of 2694 mas. If

Table 5. Proper motions, projected velocities and 'start' ($\xi = 0$) dates and phases of persistent dust emission features.

Knot	P. M. (mas yr^{-1})	Proj. vel. (km s^{-1})	Date ($\xi = 0$)	Phase ($\xi = 0$)
'C1'	326 ± 7	2860 ± 60	2001.50 ± 0.08	0.050 ± 0.011
'C0'	244 ± 9	2140 ± 76	2001.37 ± 0.14	0.034 ± 0.018
'E'	316 ± 12	2767 ± 105	2001.06 ± 0.12	0.995 ± 0.015

this is dust formed in the 1993 episode, the mean proper motion would be 232 mas yr^{-1}, close to that of corresponding feature in the 12.5 μm image and mean proper motion of 'C0' (244 ± 9 mas yr^{-1}; Table 5), so we believe this is the remnant of 'C0' formed in the 1993 dust formation episode.

3.3 Proper motions of the dust emission features

The positions of the labelled dust concentrations are used to characterize the motion of the dust clouds away from the star. As can be seen from Table 4, the PAs of 'C1' measured from our images fall in a narrow range, having an average 216° ± 2° from 19 observations over three years. The PAs of 'C0' and 'E' have averages 154° ± 6° and 112° ± 4°, respectively. The scatter in PAs is comparable to the observational uncertainties, so we believe that we are seeing the same dust concentrations in radial expansion, greatly extending the demonstration of homologous expansion of the dust from the early images by MTD. This is shown in Fig. 6, where the radial distances of 'C1', 'C0' and 'E' from the central star are plotted.

The average of the PAs measured for 'E' is very close to those of 'Feature E' given by MTD and measured by us from their published 3.08 μm image, so we believe that these are the same physical entity and included both in the fit to determine the proper motion.

We also identify a dust feature in the Keck 2.21 μm image with our concentration 'C0'. Its PA matches our mean PA for 'C0' and its radial distance fits the linear expansion (Fig. 6) found for 'C0'. We do not see it in the Keck 2.26 and 3.08 μm images observed on the same date (Tuthill et al. 2003), although the 2.26 μm image shows an E–W structure consistent with the 'bar'.

We did not plot ξ for MTD's 'Feature D' and our 'D' from the INGRID image (Fig. 3), and are not confident that they are the same entity since the dispersion in PA is much greater than those of the persistent concentrations. Also, we did not recover 'D' in any of our subsequent observations, nor did we observe concentrations corresponding to MTD's Features 'A' or 'B'.

Linear fits to the distances give the proper motions in Table 5. Those of 'E' and 'C1' are very similar, while that of 'C0' is significantly less. This could be caused by a lower physical velocity or a different inclination angle of its trajectory, which can in principle be tested by a comparison of its fading rate with that of 'C1' (Section 3.5).

We transform the observed proper motions to the transverse velocities given in Table 5 assuming a distance of 1850 pc. The proper motions of 'C1' and 'E' are close to the terminal velocity of the WC7 stellar wind (2860 km s^{-1}; Eenens & Williams 1994), but this is fortuitous: we expect the velocities of the dust grains to be the sums of their terminal drift velocities and those inherited from the wind in which they formed. The relative constancy of the proper motions points to constant terminal drift velocities in a $\rho(r) \propto r^{-2}$ environment where the acceleration and drag forces balance:

$$\rho(r)u^2 = \frac{\sigma}{c}\left[\overline{Q}_{\rm pr}(a, T_{\rm O})T_{\rm O}^4 R_{\rm O}^2 + \overline{Q}_{\rm pr}(a, T_{\rm W})T_{\rm W}^4 R_{\rm W}^2\right] r^{-2}.$$

There may be a higher density region about 800 mas from the stars in the direction of 'E', which slowed it down in 2003 as indicated by its radial distance measured from both the images observed in 2003.86. Otherwise, the constancy of the proper motions implies that the circumstellar environment through which the dust is moving does have a $\rho \propto r^{-2}$ density distribution, as produced by a constant velocity wind, with any irregularities in the interstellar medium long since swept up into the ring observed with *IRAS*.

The initial velocity of the dust must be that of the dense wind in which it condensed. The compressed wind material in a WCR flows slowly near the stagnation point and accelerates as it moves further from the stars. Cantó, Raga & Wilkin (1996) derived formulae for the velocity of the shock-compressed wind flowing in a thin shell along the contact discontinuity in terms of the wind velocities of the two stars and the wind-momentum ratio, $\eta = (\dot{M}v_\infty)_{\rm O}/(\dot{M}v_\infty)_{\rm WR}$. The asymptotic value for the velocity of the compressed WC7 wind in WR 140, using the stellar winds of the WC7 and O5 stars from Paper I and, e.g., $\eta = 0.1$ (VWA), would be 2373 km s^{-1}, about 80 per cent of the WC7 wind terminal velocity.

It is uncertain how well the 'thin shell' analytic model can describe real, turbulent wind collisions as discussed by, e.g., Walder & Folini (2002), but there is observational evidence for sub-terminal velocities of compressed WC star wind material in WCRs. Emission from such material is observed in 'sub-peaks' on the broad emission lines of low-excitation ions, notably the He I λ1.083 μm and C III λ5696 Å lines. The evolution of the profile of the latter line in WR colliding-wind systems has been studied by several authors, e.g. Lührs (1997), Hill, Moffat & St-Louis (2002) and, in the case of WR 140, MM03. The changing profile of the line as the orbits progress has been modelled geometrically in terms of emission by material flowing along the surface of a cone (approximating the WCR far from the stars) at a constant velocity, giving values for the cone opening angle and flow velocity. The flow velocities derived are typically ∼75 per cent of the wind terminal velocities, with that for WR 140 being 2300 ± 500 km s^{-1} (MM03). We therefore suggest that the dust grains formed in WR 140 had initial velocities ∼2400 km s^{-1} and were accelerated by radiation pressure to achieve their observed constant velocities. This implies drift velocities as high as ∼500 km s^{-1} through the local compressed wind, which are rather high for the survival of the grains against sputtering by He and C ions.

3.4 'Start dates' and dust formation time-scales

The abscissae (Table 5) are related to the phases at which the dust-forming plasma was initially compressed in the densest part of the WCR, near the stagnation point between the stars. The stellar winds are compressed in the WCR throughout the orbit, so we use the term 'dust-forming plasma' to refer to wind sufficiently compressed to nucleate dust as it flows further away from the stars. We refer to the dates in Table 5 as 'start dates' for convenience, but this would be true only if the concentrations had constant velocities between their formation and our first measurements. We expect the dust-forming plasma to have accelerated within the WCR and the newly formed dust to have accelerated further by radiation pressure, so the dates when the dust-forming plasma started its motion are earlier than those in Table 5 from extrapolation to $\xi = 0$. This is evident from the light curves, which showed that the nucleation of new dust was complete by $\phi = 0.03$ (Section 3.1, Fig. 2), before the extrapolated $\xi = 0$ phases of 'C0' and 'C1', the strongest dust features which would have dominated the infrared photometry. However, the interval between the first ('E') and last ('C1') start dates (0.055 ± 0.018 P) is about twice the duration (0.03 P) of dust nucleation inferred from the light curves. Although the intervals can be reconciled within the errors, the difference suggests that the delays between compression of the dust-forming plasma and dust nucleation are different for the different features. The alternative is that the timing of the 2001 eruption was different from the 1985 and 1993 events, on which the light curves are based. We do not have an infrared light curve for the 2001 eruption, but the timing is loosely constrained by the 2000.69 mid-IR photometry, showing that dust formation had not started at $\phi = 0.95$, and the 2001.25 near-IR photometry

showing dust emission at $\phi = 0.02$. Also, we know from the dilution of the emission lines in the IR spectra observed by VWA that dust formation began some time between 2001 January 3 and March 26 ($\phi = 0.989$–0.017), and that between April 28 and May 21 ($\phi = 0.028$–0.036) the near-IR emission was fading, indicating that nucleation had stopped. This is consistent with the previous eruptions. Also, the longer wavelength images (Fig. 5, Section 3.2) showing dust features from the 1993 eruption located at the same PAs as the strongest features 'C0' and 'C1' from the 2001 eruption shows no reason to believe that the timing of the 2001 dust formation differed from those of the previous episodes.

As the nucleation radius (∼125 au) is large compared with the dimensions of the orbit (∼16 au), the flow times will not vary significantly with the movement of the WCR with phase. The implication of the difference in delays is that nucleation does not always occur as soon as the dust-forming plasma reaches the nucleation radius. If it is the case that the nucleation of the earliest dust occurred less promptly than that of 'C1' or 'C0', thereby shortening the nucleation interval, the acceleration of the older dust by radiation pressure would also have been delayed, and its 'start date' would have been even earlier. This is considered further when we compare the distribution of dust around the star with the projected motion of the WCR around the orbit.

3.5 Photometry from the images

Contemporaneous imaging at different wavelengths allows the estimation of the IR colours of the circumstellar features relative to those of the star. We measured the fluxes using software apertures on the images. The results from such photometry must be viewed with caution because, as Monnier (2003) points out, the photometry of MEM-reconstructed images is necessarily biased, leading to a systematic lowering of the estimated fluxes of compact sources. We used a small aperture (typically 0.5 arcsec) on the star excluding, as far as possible, the dust emission to calibrate the images and a larger aperture, including the stellar and dust emission ('System'), to simulate the conventional photometry for a consistency check. As the system evolved, we used successively larger apertures for the 'System' and dust features but always took care to match the positions and numbers of pixels included in the corresponding aperture on each set of images observed at the same epoch to get the best estimate of the colours. In addition to 'C0' and 'C1', measured through 0.4–0.5 arcsec apertures, we included them and the emission between them in a 'bar' aperture, increasing from 0.8 × 0.3 arcsec (E–W × N–S) at phase 0.23 to 1.5 × 0.4 arcsec at phase 0.56. Most images show emission between 'C0' and 'C1', sometimes concentrated in a knot, suggesting that the 'bar' is a single structure having two to three regions of higher (projected) density, perhaps emphasized in the images by the reconstruction process. This is supported by the close similarity of the 'start' dates of 'C0' and 'C1', and not ruled out by the difference in their proper motions. We also used rectangular apertures to measure flux from the 'arm', increasing from 0.3 × 1.0 arcsec (E–W × N–S) at phase 0.23 to 0.4 × 1.7 arcsec at phase 0.46. These included 'E', which appears from its earlier 'start' date to be a separate structure formed earlier. This is consistent with the Keck images, which show a tight concentration south of the star and a more diffuse one to the east, about 120 mas more distant from the stars.

The results from the UIST images are given in Table 6, showing that all the features are significantly redder than the star, as expected from heated circumstellar dust. In the seven months between the $\phi = 0.23$ and 0.29 observations, the emission from the features fades relative to the star and, in most cases, becomes redder, as expected from cooling dust. The (nbL'–[3.99]) colours in the 2003 June image appear to be anomalously red, being comparable to those from the 2004 June image observed a year later, and much greater than those from the 2002 November image, probably due to the problem with the reconstruction of the 2003 nbL' image.

Table 6. Photometry from the UIST images through software apertures centred on the star and various dust emission features. The 'System' aperture was centred on the star and aimed to include stellar and emission feature fluxes. The apertures for the 'Bar' and 'Arm' were rectangular and their dimensions are given in the text. The nbL', [3.99] and M' magnitudes and the colours are given relative to the central star.

Feature	Phase	nbL'	[3.99]	M'	(nbL' –[3.99])	([3.99] –M')
Star		0.0	0.0	0.0	0.0	0.0
'C1'	0.23	1.0	0.5		0.5	
'C1'	0.29	2.0	1.3		0.7	
'C1'	0.43	3.7	2.9	2.8	0.8	0.1
'C1'	0.46		3.1	2.9		0.2
'C1'	0.56		3.9	3.6		0.3
'C0'	0.23	0.7	0.3		0.4	
'C0'	0.29	2.2	1.3		0.9	
'C0'	0.43	3.4	2.8	2.5	0.6	0.3
'C0'	0.46		3.2	2.8		0.4
'C0'	0.56		3.9	3.5		0.4
'Bar'	0.23	-0.1	−e0.5		0.4	
'Bar'	0.29	1.2	0.4		0.8	
'Bar'	0.43	2.3	1.7	1.6	0.6	0.1
'Bar'	0.46		1.9	1.6		0.3
'Bar'	0.56		3.0	2.3		0.7
'Arm'	0.23	2.0	1.6		0.4	
'Arm'	0.29	2.6	1.9		0.7	
'Arm'	0.43	5.2	3.4	3.9	1.8	−0.5
'Arm'	0.46		3.2	2.8		0.4
System	0.23	−1.0	−1.2		0.2	
System	0.29	−0.4	−0.7		0.3	
System	0.43	−0.2	−0.3	−0.3	0.1	0.0
System	0.46		−0.4	−0.4		0.0
System	0.56		−0.1	−0.2		0.1

We observed the fluxes from 'C0' and 'C1' to test from their relative cooling rates whether their significantly different proper motions are caused by differences in the inclination angles of their trajectories or real differences in expansion velocity. If the 75 per cent lower proper motion of 'C0' is attributable to a lower velocity, 'C0' would always be closer to the stars. The dust temperature is expected to fall off as $T_g \propto r^{-0.38}$ (Section 3.1) so the dust in 'C0' should be about 12 per cent hotter than that in 'C1'. This leads to an emissivity ratio varying from 1.8 to 2.2 at 3.99 μm (the wavelength at which most observations are available) as the dust cools so that, whatever the ratio of dust masses in 'C0' and 'C1', the [3.99] magnitude difference between the concentrations should widen as the dust fades. The fading of the [3.99] magnitudes of 'C1' and 'C0' is compared in Fig. 7 and there is no evidence that 'C1' is fading more quickly.

Modelling the (nbL'–[3.99]), ([3.99]–M') and ([7.9]–[11.5]) colours for the relevant temperatures leads us to expect that 'C0' should be ≃0.1 mag bluer than 'C1' if it were moving more slowly, but the observed colours (Tables 6 and 7) do not support this: (nbL'–[3.99]) are bluer, ([3.99]–M') are redder and ([7.9]–[11.5]) are the same. We therefore consider it more likely that 'C0' and 'C1' are

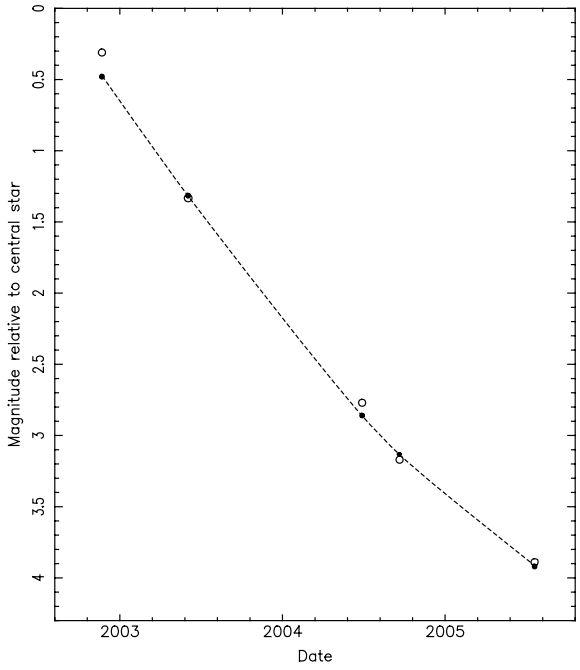

Figure 7. Comparison of [3.99] magnitudes of 'C1' (• and broken line) and 'C0' (○) relative to the central star.

Table 7. Photometry of features and the star+dust system from the Gemini images. The [7.9], [12.5] and [18.5] magnitudes and ([7.9]–[12.5]) colour are relative to the central star.

Feature	Phase	[7.9]	[12.5]	[18.5]	([7.9]–[12.5])
Star		0.0	0.0	0.0	0.0
'C1'	0.35	0.8	1.1		−0.3
'C1'	0.36	0.9	1.1	1.3	−0.2
'C0'	0.35	0.4	0.7		−0.3
'C0'	0.36	0.6	0.8	1.2	−0.2
'Bar'	0.35	−0.4	−0.1		−0.3
'Bar'	0.36	−0.4	−0.1	0.2	−0.3
'Arm'	0.36	1.2	1.4	1.3	−0.2
System	0.36	−1.2	−1.0	−0.9	−0.2

at the same temperature and distance from the star, and that the difference in proper motion, is attributable to a difference in the inclination angles of their trajectories to our line of sight. This does not rule out the possibility that they might be concentrations in the same physical structure.

The dust photometry can be calibrated via the star. From the pre-outburst photometry (Section 3.1), we used $M' = 4.53$ and $[12.5] = 3.25$, and interpolated $nbL' = 4.85$, $[3.99] = 4.75$ and $[7.9] = 3.95$ for the dust-free star. The System (star+dust) magnitudes provide a consistency check. For example, the differences in Table 6 give System magnitudes $nbL' = 3.9$ and $[3.99] = 3.6$ in 2002 November ($\phi = 0.23$) and $nbL' = 4.4$ and $[3.99] = 4.0$ in 2003 June ($\phi = 0.29$), which compare well with the $L' \simeq 3.93$ and 4.15 for these two phases on the photometric light curve. Similarly, the differences in Table 7 give System magnitudes $[7.9] = 2.7$ and $[12.5] = 2.2$ at phases 0.33 and 0.34, consistent with the photometry at phase 0.34: $[8.75] = 2.8$ and $[12.5] = 2.3$. As noted above, the calibrated 2004–05 UIST images gave M' magnitudes of the combined system in excellent agreement with the *M*/*nbM* light curve. They agree also with the System magnitudes derived from the pre-outburst calibration and the differences in Table 6.

The imaging observations cover too short a baseline in wavelength for determining the temperature of the dust, but we can check for consistency using the average dust temperature derived from fitting the 2–20 μm SEDs. At phase 0.26 (between the 2002 and 2003 imaging observations), the fit gave $\langle T_g \rangle \simeq 700$ K and emission from dust at this temperature has (nbL'–[3.99]) = 0.35, which is 0.25 mag redder than the star. The (nbL'–[3.99]) differences from the 2002 November ($\phi = 0.23$) image are slightly greater than this, but those from the 2003 June ($\phi = 0.29$) image significantly greater, as noted above. The final UIST image was also observed at a phase ($\phi = 0.56$) close to one at which we have a photometry out to 20 μm. That SED gives $\langle T_g \rangle \simeq 530$ K, which has ([3.99]–M') = 0.6, reasonably consistent with the differences in Table 6.

Photometry through software apertures on the Michelle images is given in Table 7. Counter-intuitively, the dust is *bluer* in ([7.9]–[12.5]) than the star. This is correct. It occurs because, at the time of the observations, the dust emission peaked at a wavelength shorter than those of the observations, and the Rayleigh–Jeans tail of the Planckian dust spectrum is steeper than the spectrum of the free–free emission from the stellar wind. From fitting the 3.5 to 20 μm SED for phase 0.34, we get $\langle T_g \rangle \simeq 600$ K, giving a model colour ([7.9]–[12.5]) $\simeq 0.25$. From the pre-outburst photometry (Section 3.1), we interpolate ([7.9]–[12.5]) = 0.75 for the star, which is about 0.5 mag redder than the dust features, comparable with our images (Table 7). The calibrated System colours from the images are ([7.9]–[12.5]) = 0.5–0.6, consistent with the ([8.75]–[12.5]) = 0.5 observed at phase 0.33.

We examined the evolution of the dust mass in the most persistent feature, the 'bar', and used the [3.99] magnitude in Table 6, the longest data set and at a wavelength near the dust SED peak. We calculated dust emissivity from grain temperatures T_g estimated by interpolating amongst the $\langle T_g \rangle$ determined from fitting the multi-band *H* to [19.5] data at those phases at which the photometry over the full wavelength range was available. The 'bar' dominates the dust emission, so this should give reasonable estimates of its temperature. The relative dust masses derived (Table 8) are independent of grain emission coefficient but do rely on the star being constant at 3.99 μm. They show that the mass of dust falling steadily during the period covered, but at about twice the rate at which the total dust mass was found to fall in the same phase interval from modelling the photometry (cf. Section 3.1) to which the 'bar' flux makes a significant contribution. This suggests that, as the dust emission fades to approach the noise level in the images, we are progressively losing flux in the reconstructed images and that the reduction of dust mass in Table 8 is an overestimate.

The emission from the dust 'arm' is fainter than that from the 'bar' in all the images in which emission from both could be measured, pointing to a lower mass of dust in the 'arm'. The emissivity will also be lower if the dust is cooler than that in the 'bar', which will be the case if it is more distant from the stars, as is suggested by the projected distances of the features (Table 4). This is supported

Table 8. Evolution of the relative dust mass, M_d, in the 'bar', along with the measured [3.99] difference and adopted temperature.

Date	Phase	[3.99]	T_g	Rel. M_d
2002.89	0.23	−0.50	730	1.00
2003.42	0.29	0.44	665	0.68
2004.49	0.43	1.71	565	0.55
2004.71	0.46	1.87	555	0.54
2005.52	0.56	2.98	530	0.26

by the (*nbL*′–[3.99]), ([3.99]–*M*′) and ([7.9]–[12.5]) colours of the 'arm', which are slightly redder or the same as those of the 'bar'. The baselines are too short to determine grain temperatures from fitting the colours, so we use the radiative equilibrium temperature ratios, $T_g \propto r^{-0.38}$, assuming that the ratios of the distances of the 'arm' and 'bar' from the stars was equal to that of the projected distances (Table 4) measured from the images, to estimate temperatures. We use these to form synthetic colours and check them for consistency with those observed.

The projected distances of 'E' and 'C1' at the times of the 2002 and 2003 UIST observations suggest that the dust in the 'arm' would be about 50 K cooler than that in the 'bar'. This would account for only 0.4 mag of the difference in [3.99] and 0.04 mag in (*nbL*′–[3.99]). The colour difference is consistent with those in Table 6. The balance of the flux differences from the 2002 and 2003 observations suggests that mass of dust in the 'arm' was lower than that in the 'bar' by a factor of $\simeq$4. Similarly, we get a 40 K difference in 'bar' and 'arm' temperatures at the time of the 2003 Gemini observations, accounting for 0.23 mag of the difference in [7.9] and 0.07 mag in ([7.9]–[12.5]). The measured differences in ([7.9]–[12.5]) are greater (0.1 and 0.2 mag; Table 7), implying a greater temperature difference, for which we adopt 60 K. This accounts for 0.35 mag (at 7.9 μm) of the differences between 'bar' and 'arm' fluxes. The balance of the measured flux differences indicates a lower dust mass in the 'arm', by a factor of $\simeq$3. Finally, a 50 K difference in 'bar' and 'arm' temperatures at the time of the 2004 September UIST observation would account for 0.7 mag of the difference in [3.99] and 0.09 mag in ([3.99]–*M*′). The latter is consistent with the observed colours (Table 6) and the balances of the measured [3.99] and *M*′ differences give a dust mass ratio of $\simeq$4. Owing to the possible loss of flux in the fainter reconstructed images, this ratio is probably overestimated; but all the observations, going back to the 2002 images, point to fainter dust emission in the 'arm' so there is certainly some mass difference.

The distances of the dust features from the 1993 dust formation episode, 'F' and 'G' observed with Gemini at 12.5 μm (Fig. 5), are about 4.1× those of 'C0' and 'C1', giving radiative equilibrium temperatures $\langle T_g \rangle \simeq 350$ K for 'F' and 'G'. At 12.5 μm, such dust has an emissivity about 19 per cent that of the 600 K dust from the 2001 episode. If the mass of dust in 'G' was the same as that in the corresponding feature, 'C1', it would be 1.8 mag fainter. The observed magnitude difference is nearer 3.4 mag, suggesting that much of the dust from the 1993 episode has been lost, consistent with the fall in the mass of dust in the 'bar', but this effect may be overestimated as noted above given the faintness of the emission. Similarly, the corresponding feature in the 2004 September UIST *M*′ image would have $\langle T_g \rangle \simeq 340$ K and an emissivity at this wavelength of only 1 per cent that of the 550 K dust from the 2001 episode. A comparison with the measured magnitude difference suggests that half of the original dust had been lost but this is very uncertain. The emissivity ratio at shorter wavelengths is even less, only 0.5 per cent at 3.99 μm, accounting for our not observing the '1993' dust in the [3.99] images.

4 RELATION OF THE DUST IMAGES TO THE ORBIT AND CWB PARADIGM

4.1 Changing configuration of WR 140 during dust formation

The CWB paradigm has dust forming from the compressed wind in the WCR and expanding radially from the stars. The WCR at large distances from the stars may be approximated by a hollow cone of

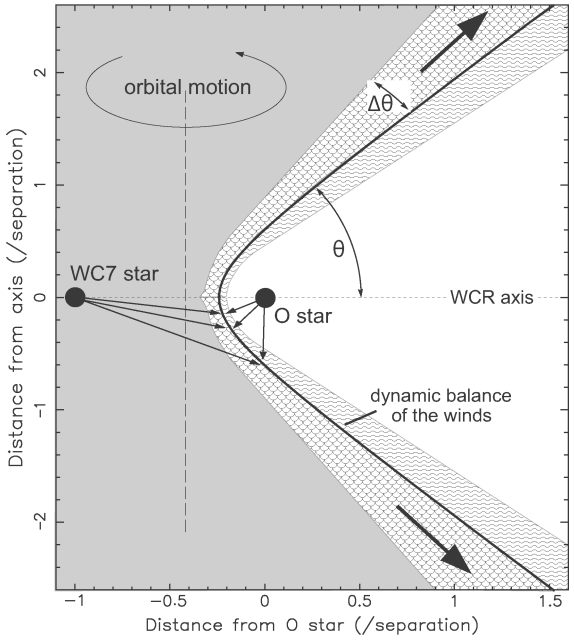

Figure 8. A sketch of the WCR relative to the stars; the observer is in the plane of the orbit, perpendicular to the WCR axis. The winds of the WC7 and O stars are separated by a contact discontinuity approximated at large distances by a cone whose opening angle, θ, depends on the ratio of the momenta of the two winds. On either side of it are surfaces where the WC7 and O stellar winds are shocked. This effect diminishes in the outer regions of the WCR as the angles of incidence of the undisturbed WC7 and O5 winds on the WCR get smaller. Note that our definition of $\Delta\theta$ differs from that of Eichler & Usov (1993), which includes the shocked regions on both sides of the contact discontinuity.

opening angle θ and thickness $\Delta\theta$ (cf. Fig. 8), following analytical models of, e.g., Eichler & Usov (1993) and Cantó et al. The WCR is assumed to be symmetric about its axis, the line of centres of the stars. The dust extends $(\theta+\Delta\theta)$ above and below the orbit, and this quantity could be determined directly from observations if the orbit was highly inclined. The WCR moves with the stars in their orbital motion, spreading the dust round the stars, and would produce a 'pinwheel' if the dust formation was continuous. In the case of WR 140, which makes dust for only a small fraction of its period, the distribution of dust in the plane of its orbit is determined by $(\theta+\Delta\theta)$ and the angular movement of the WCR during the phase interval when the WCR was producing dust-forming plasma (i.e. suitably compressed wind), and we expect to observe only an arc of a dust pinwheel. After determining the orientation of the orbit on the sky, Dougherty et al. (2005) noted that the O5 star was NW of the WC7 star at the time of periastron, and commented on the paucity of dust in that direction, where they expected dust to form. Indeed, our images show the dust to be located in a number of clouds spread most of the way around the stars, but not to the NW, where it was seen only in the early Keck images of MTD.

Owing to the high orbital eccentricity (0.881; MM03), the PA of the WCR changes very rapidly around periastron passage, so that the placement of the dust plume around the system is particularly sensitive to the timing of the production of the dust-forming plasma. For example, the PA of the O5 star relative to the WC star moves through more than one-quarter of its orbit, from 356° to 246°, in only 0.01 P ($\phi = 0.995$–0.005), and through three-quarters of its orbit in only 0.04 P. These ranges are very sensitive to the orbital eccentricity itself, because it is so high. They account for the spreading of the

dust around much of the orbit despite the short duration of dust formation.

Another consequence of the highly variable orbital velocity around periastron is that the density along the plume varies sharply with PA. Even if dust forms at a constant rate, the density on the sky of dust condensed from dust-forming plasma originating at periastron is more than 10 times lower than that originating at phase 0.02, where the WCR sweeps round more slowly, and the dust is spread less thinly.

4.2 Modelling the dust distribution

As a baseline, we model the distribution of dust made by WR 140 according to the CWB paradigm. For each phase between the start and end phases (or the phase of the model if that occurs sooner), we calculate the orientation of the WCR from the orbital elements of MM03 and Dougherty et al. The dust formed at that phase will form a ring whose location, size and orientation are defined by extending the WCR away from the stars in proportion to the interval since the start phase. This ring is then projected on a 200 × 200 grid on the sky to build up a 2D map of the dust, which can be translated directly into emission as the dust is optically thin in the IR (Paper I). For comparison with observations, the dust map is convolved with a Gaussian profile.

Besides the orbit, the principal parameters determining the dust distribution are the shape of the WCR and duration of the process. Other parameters are the efficiency with which dust nucleates from the plasma, the density distribution around the WCR and the velocity of the dust.

The shape of the WCR is determined by the dynamical balance of the two stellar winds at the contact discontinuity. From the stagnation point on the axis, where the winds collide head-on, the WCR curves until, further from the stars, it can be approximated by a cone. If the stellar winds have reached their terminal velocities before collision, the value of the opening angle, θ, depends only on the wind-momentum ratio, $\eta = (\dot{M}v_\infty)_{\rm O5}/(\dot{M}v_\infty)_{\rm WC}$, and does not vary with stellar separation around the orbit. In this case, the shape of the WCR would remain the same while its proximity to the stars varied with the stellar separation. From consideration of the mass-loss rates of the WC7 and O5 stars based on X-ray and radio observations at $\phi = 0.837$, Pittard & Dougherty (2006) derived a wind-momentum ratio $\eta = 0.02$, which gives $\theta = 31^\circ$. From spectroscopic observations near periastron, MM03 determined $\theta = 40 \pm 15^\circ$ from modelling the moving sub-peaks on C III and He I emission lines, and VWA found $50^\circ < \theta < 60^\circ$ (for $i = 122^\circ$) from the orbital variation of the absorption component of the λ1.083 μm He I line. We begin by adopting, as a round number, $\theta = 40^\circ$, corresponding to $\eta = 0.046$.

Near periastron, the distance from the O5 star to the stagnation point is given by

$$r_{\rm O5} = \frac{\sqrt{\eta}}{\sqrt{1+\eta}} D,$$

where D is the stellar separation (Eichler & Usov), and could become too small for the O5 stellar wind to have accelerated to its terminal velocity before collision. At periastron, $D = 0.12a$ and, if $\eta = 0.046$ and $R_{\rm O5} = 26\,{\rm R}_\odot$ (as above), we have $r_{\rm O5} = 2.9\ R_{\rm O5}$. For a simple β wind velocity law of the form

$$v(r) = v_\infty \left(1 - \frac{R_{\rm O5}}{r}\right)^\beta,$$

the O5 wind velocity would be only $0.66\,v_\infty$ (assuming $\beta = 1.0$) when it reached the WCR at $r = r_{\rm O5}$, and the WCR would contract around the O5 star, with a smaller opening angle, θ. The effect would be greater for a smaller wind-momentum ratio, e.g. $v(r_{\rm O5}) = 0.5\,v_\infty$ for $\eta = 0.02$. Countering this effect is the possible radiative braking of the WC7 wind by the O5 star's radiation field, normally insignificant in WR 140 (Gayley, Owocki & Cranmer 1997), which might occur as the WCR moves closer to the O5 star, so that a wind-momentum balance could still exist. Detailed modelling of the WCR under these conditions is beyond the scope of the present study; for which we recall the persistence of the C III sub-peak emission right through periastron (MM03), and of dust nucleation as suggested by the K-band photometry (Fig. 2), which indicate that the WCR does not collapse on to the O5 star. Given that the effects of incomplete acceleration of the O5 wind and radiative braking of the WC7 wind work in opposite directions, we assume θ to be constant during dust formation. Consequently, the fraction of the WC7 stellar wind going into the WCR and becoming available for dust formation would be independent of phase. We also assumed that the fraction of compressed wind that condensed dust was constant while this phenomenon occurred, i.e. that dust nucleation was a threshold phenomenon.

The appropriate value of $\Delta\theta$ is unknown: Pittard & Dougherty (2006) found values of $\Delta\theta \simeq 20^\circ$ for a range of possible values of θ, but this applies to adiabatic post-shock winds. Where there are radiative losses, which is the case with WR 140 near periastron (MM03; VWA), $\Delta\theta$ will be smaller (Eichler & Usov 1993), and we arbitrarily adopt $\Delta\theta = 10^\circ$ here for this phase range. In principle, it could be much thinner, but instabilities from cooling could again increase its geometrical thickness (Folini & Walder 2002).

The WCR moves with the stars in their orbit, the axis lagging behind the line of centres because of the orbital motion. Owing to the high eccentricity, the aberration angle, $\delta = \arctan(v_{\rm orb}/v_{\rm wind})$, resulting from the Coriolis force varies significantly round the orbit with the varying transverse velocity of the WCR, $v_{\rm orb}$, taken to be that of the WCR relative to the WC7 star. Owing to the long orbital period and fast stellar winds in WR 140, δ is expected to be small and only reach 5° at periastron. This is smaller than the corresponding angle $\delta\phi = 40^\circ \pm 20^\circ$ (assumed constant) found from fitting the emission-line sub-peaks (MM03), and we used the aberration angle from the transverse velocity in our modelling.

The distribution of compressed wind and dust around the axis of the WCR is unknown. Models of an adiabatic WCR in γ Vel show a greater density enhancement in the trailing edge (in the orbital plane) of the WCR than in the leading edge, and this was predicted to carry over to the radiative case (Folini & Walder). Similarly, Lemaster, Stone & Gardiner (2007) found higher densities on the trailing edges of the WCR in their study of the effects of the Coriolis force on CWB interactions but, as none of these models was directly applicable to the case of WR 140, we began by assuming an axisymmetric density distribution and consider deviations below.

The compressed wind accelerates in the WCR from the stagnation point to the cone-shaped region, where it reaches an asymptotic velocity of about 80 per cent that of the stellar winds (Section 3.3). The wind is assumed to continue ballistically on this trajectory. During some interval, dust condenses in the down-stream flow and is quickly accelerated by radiation pressure to its terminal drift velocity.

As discussed in Section 3.4, there are two sets of data determining the orbital phases at which the WCR started and ceased to produce dust, each with its own assumptions and delays. On the one hand are the $\xi = 0$ abscissae in Table 5, which are later than the true dates owing to the acceleration of the dust-forming plasma in the WCR, and then of the dust grains by radiation pressure. If these

delays are the same for all dust features, the differences between the $\xi = 0$ dates still hold, i.e. 'E' and the 'arm' were formed first, followed 0.039 ± 0.023 P and 0.055 ± 0.019 P later by 'C0' and 'C1'. The interval between the last two features is comparable to the uncertainties, and they may have been formed at the same time, which is compatible with the clockwise rotation of the system on the sky. On the other hand are the phases at which the near-IR light curves showed dust nucleation to be occurring ($\phi \simeq 0.0$–0.025; Section 3.1), giving half the duration.

We begin by adopting the time-scale indicated by the proper motions. If the production of dust-forming plasma depends only on conditions such as local radiation field and pre-collision wind density, which depend on stellar separation, the 0.055 P phase interval would occur symmetrically about periastron, i.e. running from $\phi = 0.972$ to 0.028 (80 d before and after periastron passage) when the local conditions would have been the same. We assume that, between these phases, the rate of compression of the dust-forming plasma was constant. We are aware that this runs counter to the observation that the mass of dust formed before periastron, the 'arm', is about one-quarter that formed afterwards but, in the absence of an obvious physical reason for this difference, continue with our assumption.

Using these parameters, we constructed a specimen model of the dust clouds for $\phi = 0.18$, near the time of the 2002 July observations. A comparison of the model (Fig. 9) and observed dust images (Fig. 3) shows that the model reproduces the southern 'bar', including the concentrations 'C0' and 'C1', reasonably well, but not the eastern 'arm', and produces more dust to the northwest than seen in the observations. Owing to the high angular velocity of the WCR around periastron, the angular distribution of dust is very sensitive to the choice of interval during which dust-forming plasma is produced. The placement of dust on the sky provides tight constraints on the orientation of the WCR when the dust-forming plasma was condensed and hence on the phases at which this process occurred. In particular, images using the duration of dust nucleation indicated by the light curves (40 d before and after periastron) are a very poor fit (cf. Fig. 10). Indeed, the fit can be improved slightly by increasing the production duration of dust-forming plasma by ∼0.01 P, or by adopting a higher orbital eccentricity, which increases the PA range covered in the same phase interval, but the discrepancy between model and observed dust to the NW of the stars requires re-examination of the input assumptions.

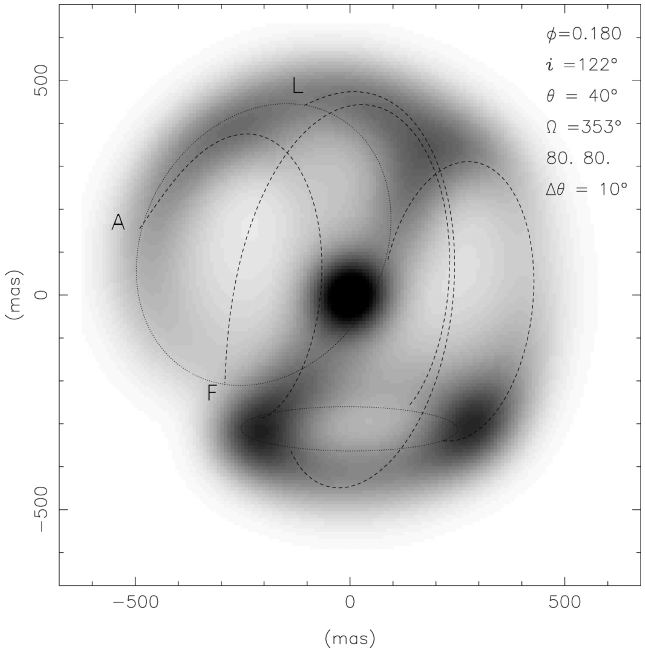

Figure 9. Model dust image for $\phi = 0.18$, near the epoch of the 2002 July observations (Fig. 3), convolved with a Gaussian of 120 mas FWHM. The stellar image is attenuated to allow the display of the dust emission. Superimposed is a frame comprising ellipses marking the projections of those regions of the WCR which the earliest (NE of the star) and latest (S of the star) dust to form would have reached by the model phase ($\phi = 0.18$) and, joining them, arcs showing the loci of four points on these ellipses, that at the leading edge of the WCR in the orbital plane (marked 'L'), the following edge ('F'), and maxima above ('A') and below (these are arbitrary) the plane. The dust is optically thin, so we see the superposition of dust made at different phases and limb brightening of hollow structures.

The model dust NW of the stars is not dust formed at periastron; dust from wind compressed around periastron would be spread with PA extending $\pm 50^\circ$ ($\theta + \Delta\theta$) on either side of the projected PA at periastron. We tested this with a variant of the model which allowed for a brief pause in dust formation very close to periastron, not long enough to show up in the light curve (Fig. 2), as if the WCR was temporarily unable to produce dust owing to the proximity of the stars or weakening of the wind collision, but this did not remove the dust to the NW. With the aid of the overplotted wire frame in Fig. 9, we see that the model dust to the NW is attributable to the overlay of dust formed in the leading edge of the WCR before periastron and, to a lesser extent, the following edge after periastron. The observed paucity of dust in this direction suggests that we abandon the assumption that the dust is distributed uniformly around the axis of the WCR. This asymmetry could be related to the asymmetries found in WCR models referred to above, or it could be a consequence of asymmetry in the WC7 stellar wind such that the WCR moved through a region of rapidly falling wind density between $\phi \simeq 0.95$ and periastron, as if there were a high-density flattened region having PA $\simeq 100^\circ$. A flattened wind for the WC7 star was proposed by White & Becker (1995) to explain the variations in the radio emission, but this is not supported by polarimetric observations (MM03 and references therein). Also, the WCR would cross such a disc a second time 180° later in PA ($\simeq 280^\circ$), leading to enhanced dust formation between PAs 240° and 320° – which is not observed.

We therefore ascribe the asymmetry to the WCR itself, and test this with the simplest parametrization of non-uniform wind density around the WCR: a fraction A of the dust is re-distributed around the axis of the WCR as $A\cos(\zeta)$, where $\zeta = 0$ is the azimuthal angle corresponding to the trailing edge of the WCR in the orbital plane. A model image with this adjustment for $A = 0.9$ is presented in Fig. 10. Although this does not reproduce the 'arm', it represents an improvement over the uniform distribution model, and might be improved further with a physically more realistic azimuthal density distribution.

The model images (Figs 9 and 10) show dust projected against the star. This is the earliest dust to form, made from the WCR when its axis was pointing towards us. This dust therefore lies in our line of sight to the stars, and is most probably that responsible for the optical eclipses observed by MM03 and previous observers shortly after periastron.

5 DISCUSSION

The unprecedented combination of high-resolution infrared imaging, multi-band infrared photometry and knowledge of its distance and the binary orbit in three dimensions provides a unique

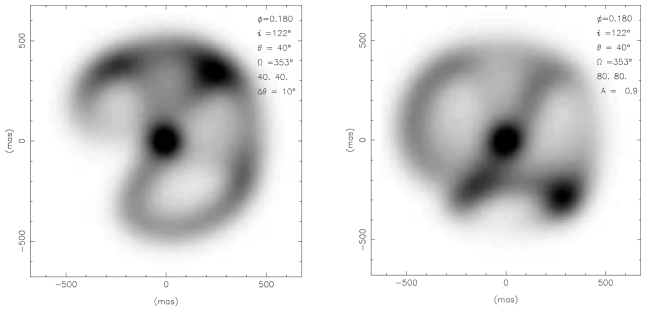

Figure 10. Model dust images for $\phi = 0.18$, showing the effects of (left) half the duration of dust formation (±40 d, from the nucleation time) and (right) an asymmetric dust distribution with $A = 0.9$. Other parameters are the same as in Fig. 9.

opportunity to examine the dust formation process by WR 140 and assess some of the underlying assumptions, with implications for other, less well observed, dust-making Wolf–Rayet systems.

Consideration of the radiative equilibrium on the youngest dust and the projected distances of the dust features from the mid-2001 images suggests that the optical properties of the grains formed by WR 140 differ from those made by the WC9 stars, particularly the classical 'pinwheel' WR 104 modelled by Harries et al. (2004), in having a lower ratio of UV-to-IR absorption coefficients. The physical conditions under which WR 140 makes dust differ from those in WR 104 – e.g. the stronger UV radiation field, as both components of WR 140 are hotter than the stars in WR 104 – so such differences are unsurprising, and recall those in different samples of carbon grains formed in the laboratory (Andersen et al.). We also recognize from the comparison of their detailed observations of the WR 104 dust plume by Tuthill et al. (2008) with the model developed by Harries et al. (2004) that the dust models based on radiative equilibrium in the stellar radiation field need refinement.

The images of the dust made by WR 140 are very different from the classical 'pinwheels' around the persistent dust-makers, more akin to 'splashes', with patches of dust at similar distances and having a variety of PAs, moving away from the stars at constant rates. Extrapolation of the motions back to the stars suggests that the dust-forming plasma responsible for the features to the east was condensed about 0.055 P before that responsible for the features to the south, assuming that the acceleration was the same for all features. The spreading of the dust around most of the orbit can be reconciled with the formation of dust in a WCR rotating with the stars and the short duration of the production of the dust-forming plasma (0.055 P) by noting that the high eccentricity of the orbit causes the PA of the WCR to swing through almost two-thirds of its orbit (233° from NE to S) in this interval. This is consistent with the dust to the E being formed before that to the S.

Calculations of model dust distributions on this basis have mixed success. They reproduce the most persistent dust feature, the southern 'bar' with concentrations 'C0' and 'C1' at the two ends, but fail to the north and east. We have examined the effects on the images of changing model (e.g. θ) and orbital parameters: most have little effect, apart from the orbital eccentricity and the phase range during which dust-forming plasma was produced. Owing to the rapid movement of the orientation of the WCR near periastron, the model images are very sensitive to the choice of the phases at which dust-forming plasma was condensed, and this provides a third, perhaps the tightest, constraint on the time-scale of dust formation. It is possible that current RV studies of WR 140 will lead to small changes to the orbital parameters but these will have to fit other constraints, such as the closely timed X-ray eclipse at conjunction (Pollock et al. 2005, fig. 1). If we drop the assumption that the acceleration of the plasma in the WCR was the same for all the dust features, the phase at which wind compression began to be sufficient for dust formation could have occurred earlier. There is no scope for a similar adjustment to the phase for the end of dust formation, as the proper motion 'start date', assumed delay and PA on the sky are consistent.

As discussed in Section 3.4, the duration of dust nucleation was half the formation interval indicated by the proper motions. Unsurpisingly, model dust images (Fig. 10) using the nucleation interval for the duration of dust formation gave worse fits to the observed images than those using the duration from the proper motions.

The simple model for dust formation in the WCR does not fully account for the dust observed around WR 140 whatever the choice of input parameters, so the model assumptions need further examination. We have already found that a model including an asymmetric distribution of dust around the axis of the WCR improves the fit to the observed images slightly. There is stronger evidence supporting this non-uniform azimuthal density distribution around the WCR axis: the different proper motion of 'C0' and 'C1', considered (Section 3.5) to be caused by the different inclination angles of their trajectories. The axis of the WCR was tilted away from us during the time when these features were formed, with the angle between the axis and our sightline [ψ, where $\cos(\psi) = -\sin(i)\sin(f + \omega)$, with f being the true anomaly of the O5 star in its orbit] varying over $\psi = 119^\circ - 104^\circ$ for $\phi = 0.015$–0.025. With $\theta = 40^\circ$, this has dust flowing both towards us and away from us, and having a threefold range of projected velocities on the sky. However, if the dust were distributed symmetrically around the WCR axis, because the emission is optically thin, the strongest dust emission would come from the limb-brightened edges of the cone, which would have the same projected distances from the star *whatever the orientation of the WCR cone*. In this case, we would be unlikely to observe the effects of different inclinations of the dust motions. This is confirmed by the modelling. Models of the dust emission for different phases assuming uniform azimuthal dust show that the concentrations to the south identified with 'C0' and 'C1' have the same proper motions. In the models with asymmetric dust, the proper motion of 'C0' is found to be 70 per cent that of 'C1', close to the observed value of 75 per cent (Section 3.3). The higher density in the following edge of the WCR accords with theoretical studies of WCRs in adiabatic systems; when the studies have been extended to systems like WR 140, the dust modelling should be repeated with a more realistic azimuthal density distribution than the simple one used here.

A similar asymmetry may apply to the dust made by the classical pinwheel WR 104, but will be harder to observe. Because its dust formation is continuous, there are no concentrations to track by proper motion, and the dust plume is narrower than that of WR 140 (see especially fig. 8 of Tuthill et al. 2008 for a stacked image), so it is harder to observe any structure in the pinwheel. It would be instructive to observe another pinwheel having a low orbital inclination, like that of WR 104, but a more luminous companion to the WC9 star and hence larger values of η and θ and a wider dust plume which might show a density gradient.

There is a second category of asymmetry in the dust formation by WR 140: the fourfold difference in the amount of dust formed in the features before and after periastron, and the difference in timescales. Either the wind-compression process depends on more than the local conditions – radiation field and pre-shock wind density – which depend on stellar separation only, or the difference in dust

mass in the 'arm' and 'bar' must be a consequence of a significant difference in the efficiency of dust formation from the wind.

We expect a delay between the compression of the dust-forming plasma and nucleation of the dust, to allow time for the plasma to flow to where the dust forms. If this is the nucleation radius (∼125 au), the delay would be about 0.03 P for a flow at about 2400 km s^{-1} (Section 3.3). Such a delay is consistent with the beginning of nucleation at $\phi = 0.0$ (Section 3.1) and the start phase, $\phi = 0.972$, adopted from the proper motions, so we could have dust nucleating as soon as it reached the nucleation radius. On the other hand, the cessation of nucleation between $\phi = 0.025$ and 0.03 at the latest places a tight limit on the delay, as the stop phase from the proper motions of 'C0' and 'C1', $\phi = 0.028$, and the PA of the 'bar', which is consistent with the condensation of the dust-forming plasma at the same phase, leave no time for it to flow to the nucleation radius.

If the basic model and the orbital parameters are correct, the time-scale for nucleation for the southern dust features suggests that dust is able to condense much closer to the stars than the radiative-equilibrium nucleation radius, perhaps because of screening by the compressed wind. Once some dust grains have condensed, they will themselves provide screening and facilitate further condensation. The models of line-of-sight dust clouds formed by WC9 stars (Veen et al. 1998) suggest that these clouds form closer to the stars than the persistent dust clouds located beyond the nucleation radii. Something similar may be happening in WR 140, but the fact that this occurred only at the end of the dust-forming episode, and then produced most of the dust, suggests different processes governing the formation of the early and final dust features.

Nevertheless, the basic features of dust formation by WR 140 can be ascribed to the CWB paradigm, including the spread of dust by the rotating WCR, but the processes at the start and finish of the process – which are not observed with the persistent dust formation by the WC9 stars – are still to be understood.

6 CONCLUSIONS

The images of WR 140 observed at wavelengths between 2 and 18 μm using four different instruments on four different telescopes give a consistent view of the evolution of the dust formed around the time of the 2001 periastron passage until $\phi = 0.56$. Dust is observed to be distributed most of the way round the star, more like a 'splash' than a short arc of a pinwheel like those made by WC9 stars as one might have expected from the very small fraction of the period (0.055 P) taken up by dust formation. This results from the fast angular motion of the binary and projection of the WCR on the sky around periastron as a consequence of the highly eccentric orbit.

The positions of three persistent dust concentrations were tracked, showing them to be moving away from the stars with constant proper motions. Extrapolation of the linear motions back to the stars indicates that one concentration, that to the E of the binary, was ejected about 145 d before the other two, both to the S of the binary and comprising the 'bar'. The constancy of the proper motions in the presence of strong radiation pressure indicates that the dust grains must have been accelerated to constant drift velocities relative to the dust-forming plasma. Continued movement through the plasma would have been important for the growth of the grains by implantation of C ions (cf. Zubko 1998) after nucleation ceased, so that the dust mass continued growing. The multi-band (H–[19.5]) light curves showed nucleation ceased around $\phi \simeq 0.025$–0.030 but dust mass increasing until $\phi \simeq 0.14$. After this phase, the dust mass began to fall, presumably due to the destruction of grains by spallation. The photometry of the most persistent dust feature, the southern 'bar', from the [3.99]-band images shows its mass falling by a factor of about 4 over $\phi = 0.23$–0.56 but this is probably an overestimate owing to the likely loss of faint flux from reconstructed images. Grain destruction at later phases must be less important, because we observed dust emission from the 'bar' made in the previous, 1993, dust-making episode at 12.5 and 4.68 μm at distances consistent with the proper motions of the concentrations made in the 2001 episode. This shows that, to the S at least, the dust expands freely in a low-density void, presumably that blown by the stellar winds. The dust feature to the E, the 'arm', is not as robust, and partly dissipates during our sequence of observations. The photometry of the images shows the dust mass in the 'arm' to be significantly less than that in the southern 'bar' including 'C0' and 'C1'.

Model images of the dust cloud were constructed with dust forming downwind in the WCR, and using the projected angular motion of the WCR calculated from the orbital elements. A comparison of the model images with the observations shows a reasonable match for the persistent dust features to the south of the stars, but differences to the E and NW. The effects of adjustments to model and orbital parameters were explored: only the phase at which the dust-forming plasma started to be produced and the orbital eccentricity significantly affected the fits to the E. The fit to the NW, where the models produced more dust than observed, could be improved by adopting an asymmetric distribution of material around the axis of the WCR, with highest density at the following edge of the WCR in the orbital plane. This asymmetry also accounts for the difference in proper motions of the two most persistent dust features and accords with theoretical work on colliding winds. It is the most promising development of the basic WCR dust formation model.

The shorter duration of dust nucleation interval suggests that the delay between wind compression and dust formation was different for different features. Dust does not necessarily start nucleation when the wind reaches the nucleation radius, and may even condense closer to the stars. The nucleation of dust in WC winds is still not understood, but the dust formation by WR 140 is consistent with this process occurring in a rotating WCR – as inferred for the rotating 'pinwheels' like WR 104 and WR 98a, for which stellar orbits are yet to be observed.

ACKNOWLEDGMENTS

The UKIRT is operated on Mauna Kea, Hawaii, by the Joint Astronomy Centre (JAC), on behalf of the Science and Technology Facilities Council (STFC) of the United Kingdom. The WHT is operated on Observatorio del Roque de los Muchachos, La Palma, by the Isaac Newton Group (ING), on behalf of the STFC. The Telescopio Carlos Sánchez (TCS) in the Observatorio del Teide is managed by the Instituto de Astrofísica de Canarias. We are very grateful to the Service Programme observers at UKIRT, the TCS and the ING for the Service observations of WR 140 over the years. AFJM is grateful for financial assistance to NSERC (Canada) and FQRNT (Quebec). We are grateful to Peter Tuthill for a helpful referee's report.

REFERENCES

Allen D. A., Harvey P. M., Swings J. P., 1972, A&A, 20, 333
Andersen A. C., Loidl R., Höfner S., 1999, A&A, 349, 243
Arnal E. M., 2001, AJ, 121, 413
Cantó J., Raga A. C., Wilkin F. P., 1996, ApJ, 469, 729

Cherchneff I., Le Teuff Y. H., Williams P. M., Tielens A. G. G. M., 2000, A&A, 357, 572
Colangeli L., Mennella V., Palumbo P., Rotundi A., Bussoletti E., 1995, A&AS, 113, 561
Conti P. S., Alschuler W. R., 1971, ApJ, 170, 325
Danks A. C., Dennefeld M., Wamsteker W., Shaver P. A., 1983, A&A, 118, 301
Dougherty S. M., Beasley A. J., Claussen M. J., Zauderer B. A., Bolingbroke N. J., 2005, ApJ, 623, 447
Eenens P. R. J., Williams P. M., 1994, MNRAS, 269, 1082
Eichler D., Usov V., 1993, ApJ, 402, 271
Eversberg T., Lepine S., Moffat A. F. J., 1998, ApJ, 494, 799
Folini D., Walder R., 2002, in Moffat A. F. J., St-Louis N., eds, ASP Conf. Ser. Vol. 260. Interacting Winds from Massive Stars. Astron. Soc. Pac., San Francisco, p. 605
Garcia M., Biauchi L., 2004, ApJ, 606, 497
Gayley K. G., Owocki S. P., Cranmer S. R., 1997, ApJ, 475, 786
Gehrz R. D., Hackwell J. A., 1974, ApJ, 149, 619
Glasse A. C., Atad-Ettedgui E. I., Harris J. W., 1997, Proc. SPIE, 2871, 1197
Hackwell J. A., Gehrz R. D., Grasdalen G. L., 1979, ApJ, 234, 133
Harries T. J., Monnier J. D. Symington N. H., Kurosawa R., 2004, MNRAS, 350, 565
Hayward T. L., Brandl B., Pirger B., Blacken C., Gull G. E., Schoenwald J., Houck J. R., 2001, PASP, 113, 105
Hill G. M., Moffat A. F. J., St-Louis N., 2002, MNRAS, 335, 1069
Lamontagne R., Moffat A. F. J., Seggewiss W., 1984, ApJ, 277, 258
Lemaster M. N., Stone J. M., Gardiner T. A., 2007, ApJ, 662, 582
Lührs S., 1997, PASP, 109, 504
Marchenko S. V., Moffat A. F. J., Grosdidier Y., 1999, ApJ, 522, 433
Marchenko S. V. et al., 2003, ApJ, 596, 1295 (MM03)
Marston A. P., 1996, AJ, 112, 2828
Moffat A. F. J., Robert C., 1994, ApJ, 421, 310
Monnier J. D., 2003, Rep. Prog. Phys., 66, 789
Monnier J. D., Tuthill P. G., Danchi W. C., 1999, ApJ, 525, L97
Monnier J. D., Greenhill L. J., Tuthill P. G., Danchi W. C., 2002a, ApJ, 566, 399
Monnier J. D., Tuthill P. G., Danchi W. C., 2002b, ApJ, 567, L137 (MTD)
Monnier J. D. et al., 2004, ApJ, 602, L57
Morris P. W., Brownsberger K. R., Conti P. S., Massey P., Vacca W. D., 1993, ApJ, 412, 324
Packham C. et al., 2003, MNRAS, 345, 395
Pittard J. M., Dougherty S. M., 2006, MNRAS, 372, 801
Pittard J. M., Dougherty S. M., Coker R. F., O'Connor E., Bolingbroke N. J., 2006, A&A, 446, 1001
Pollock A. M. T., Corcoran M. F., Steven I. R., Williams P. M., 2005, ApJ, 629, 482
Ramsay Howat S. K. et al., 2004, Proc. SPIE, 5492, 1160
Repolust T., Puls J., Herrero A., 2004, A&A, 415, 349
Salas L., Cruz-González I., Tapia M., 2006, Rev. Mex. Astron. Astrofis., 42, 273
Smith L. J., Norris R. P. F., Crowther P. A., 2002, MNRAS, 337, 1039
Stevens I. R., Blondin J. M., Pollock A. M. T., 1992, ApJ, 386, 265
Tuthill P. G., Monnier J. D., Danchi W. C., 1999, Nat, 398, 486
Tuthill P. G., Monnier J. D., Danchi W. C., Turner N. H., 2003, in van der Hucht K. A., Herrero A., Esteban C., eds, Proc. IAU Symp. 212. A Massive Star Odyssey, from Main Sequence to Supernova. Astron. Soc. Pac., Francisco, p. 121
Tuthill P. G., Monnier J. D., Lawrance N., Danchi W. C., Owocki S. P., Gayley K. G., 2008, ApJ, 675, 698
Usov V. V., 1991, MNRAS, 252, 49
Varricatt W. P., Williams P. M., Ashok N. M., 2004, MNRAS, 351, 1307 (VWA)
Veen P. M., van Genderen A. M., van der Hucht K. A., Li A., Sterken C., Dominik C., 1998, A&A, 329, 199
Walborn N. R., Fitzpatrick E. L., 1990, PASP, 102, 379
Walder R., Folini D., 2002, in Moffat A. F. J., St-Louis N., eds, ASP Conf. Ser. Vol. 260, Interacting Winds from Massive Stars. Astron. Soc. Pac., San Francisco, p. 595
White R. L., Becker R. H., 1995, ApJ, 289, 698
Williams P. M., 1999, in van der Hucht K. A., Koenigsberger G., Eenens P. R. J., eds, Proc. IAU Symp. 193. Wolf–Rayet Phenomena in Massive Stars and Starburst Galaxies. Astron. Soc. Pac., San Francisco, p. 267
Williams P. M., 2002, in Moffat A. F. J., St-Louis N., eds, ASP Conf. Ser. Vol. 260, Interacting Winds from Massive Stars. Astron. Soc. Pac., San Francisco, p. 311
Williams P. M., Beattie D. H., Lee T. J., Stewart J. M., Antonopoulou E., 1978, MNRAS, 185, 467
Williams P. M., Longmose A. J., van der Hucht K. A., Talevera A., Wamstecker W., Abbott D. C., Telesco C. M., 1985, MNRAS, 215, 23P
Williams P. M., van der Hucht K. A., Thé P. S., 1987, A&A 182, 91
Williams P. M., van der Hucht K. A., Pollock A. M. T., Florkowski D. R., van der Woerd H., Wamstecker W. M., 1990, MNRAS, 243, 662 (Paper I)
Williams P. M., van der Hucht K. A., Morris P. W., 1998, Ap&SS, 255, 169
Zubko V. G., 1998, MNRAS, 295, 109
Zubko V. G., Mennella V., Colangeli L., Bussoletti E., 1996, MNRAS, 282, 1321

This paper has been typeset from a TEX/LATEX file prepared by the author.